POLITECNICO
MILANO 1863

SCUOLA DI INGEGNERIA INDUSTRIALE
E DELL'INFORMAZIONE

Rotorcraft Ground Resonance Using Lyapunov Characteristic Exponents Estimated from Multibody Simulation

Tesi di Laurea Magistrale in
Aeronautical Engineering - Ingegneria Aeronautica

Author: **Gianni Cassoni**

Student ID: 952662
Advisor: Prof. Pierangelo Masarati
Academic Year: 2021-22

Abstract

The focus of this thesis is on studying the model of Ground Resonance proposed by Hammond without the linearization of the Lead-Lad angle. To assess the stability of a nonlinear dynamical system, one method that can be used is Floquet's, but this is only possible for periodic systems. The Lyapunov Characteristic Exponents (LCEs) and the Maximum Lyapunov Characteristic Exponent (MLCE) make it possible to study the rate of contraction/expansion of a generic system, to determine the stability/instability characteristics of the problem. Then the focus is shifted to applying these techniques to multibody dynamics, analyzing time histories computed using MBDyn, first by recreating the same results obtained with the Hammond model, then considering different and more complex systems, namely the Inter-Blade and Inter-2-Blade damper configurations, and finally a more complex and sophisticated system, a Tiltrotor wind-tunnel model on the verge of the whirl-flutter aeroelastic instability.

Abstract in lingua italiana

L'obiettivo di questa tesi è di studiare il modello di Ground Resonance proposto da Hammond senza la linearizzazione dell'angolo di Lead-Lag. Per definire la stabilità di un sistema non lineare un metodo utilizzato è Floquet, però non è sempre possibile usarlo, se il sistema non è periodico. Con gli esponenti caratteristici di Lyapunov e gli esponenti caratteristici massimi di Lyapunov è possibile studiare il rateo di contrazione/espansione per ottenere la stabilità/instabilità anche per sistemi caotici. Poi l'attenzione della tesi si sposta sulle possibili applicazioni attraverso il software MBDyn, prima ricreando gli stessi risultati ottenuti con il modello di Hammond non lineare poi con sistemi più complessi, per esempio la configurazione Inter-Blade, la configurazione Inter-2-Blade e infine il modello di Tiltrotor.

Contents

Introduction

Helicopter Ground resonance is a phenomenon that may develop when a helicopter has a mass imbalance in the axis of rotation of the hub and the rotor, that causes self-excited vibrations. The phenomenon happens when the helicopter is spinning with the landing gear in contact with the ground. This type of instability can lead to the destruction of the structure and cause injuries to the crew. In a modern helicopter, this rare occurrence is one of the more dangerous situations that can lead to the complete loss of the aircraft. As an example of the kind of possible destruction, Fig. 2 shows the consequence of a ground resonance occurrence on an AgustaWestland AW-109E.

Figure 1: AgustaWestland AW-109E.

Coleman [5] and then Coleman and Feingold [6] performed some of the earliest research on ground resonance, and laid the foundation for all the work that was to follow. Subsequent contributions were made by Donham, Cardinale and Sachs [3], and Lytwyn, Miao and Woitch [18], which considered both air and ground resonance. In addition, major contributions to the understanding and prediction of ground resonance on hingeless and bearingless rotors were made by US Army researchers [2, 8, 14].

Figure 2: Accident of an AgustaWestland AW-109E probably due to ground resonance, Poland - November 21, 2009 , photo from Jakub Kalinowski.

As a result of the previously mentioned investigations, occurrences of ground resonance can now be predicted for articulated, hingeless, and bearingless rotors with great accuracy. The use of linearized equations of motion has been shown to produce very accurate frequency predictions, but the damping has proven much more difficult to predict. This is particularly true for rotor systems that include elastomeric lag dampers, which exhibit highly nonlinear response characteristics. There are multiple types of analysis to study the highly nonlinear response, one of the common ones is the multiple scales separation and bifurcation analysis [7]. In this thesis, a different approach is followed, by using the Lyapunov Characteristic Exponents, as in [27], to estimate the damping of nonlinear systems.

1 | Ground Resonance Model

1.1. Hammond Model of Ground Resonance

To understand ground resonance, a classical model, which became a de-facto benchmark, was proposed by Hammond in a seminal 1974 paper [13]. A sketch of Hammond's model is presented in Fig. 1.1. The model is a simplified system of the coupled airframe and rotor blades. Other models exist, e.g., the one proposed by Kunz [16] (where the main difference is that the model has only one degree of freedom for the hub, and the constitutive laws of the dampers are nonlinear). In both cases, one damper is made inoperative to evaluate the stability of the resulting periodic problem.

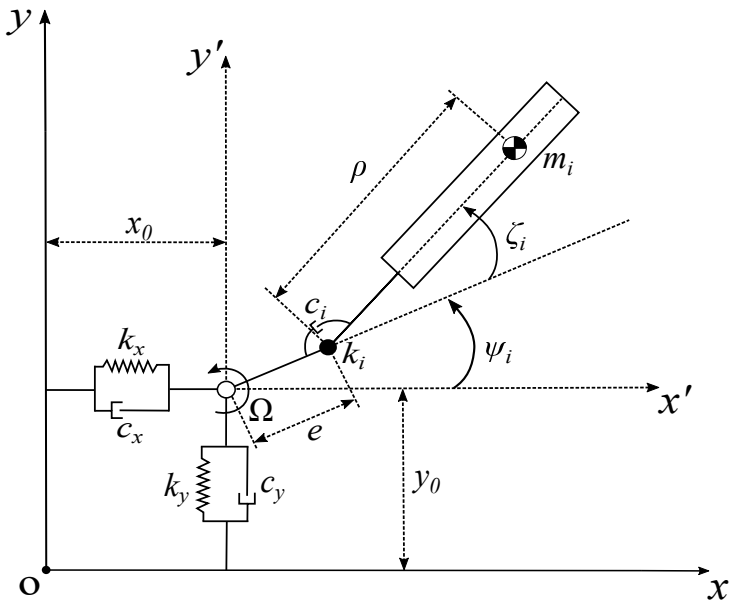

Figure 1.1: Hammond model from [13].

The equations of motion of Hammond's model are derived using an Eulerian approach. The model data are presented in Table 1.1. The degrees of freedom consist of two components of in-plane hub displacement, x_h and y_h, and a lead-lag degree of freedom, ζ_i, for each blade in the rotor (in Hammond's work four blades are considered). Each blade is

assumed to have a rotational spring and damper which act about the lag hinge. The blade equations are developed by summing the moments about the lag hinge. The displacement of a point at spanwise distance ρ from the hinge of the ith blade is

$$\begin{cases} x_i = x_h + e\cos(\psi_i) + \rho\cos(\psi_i + \zeta_i) \\ y_i = y_h + e\sin(\psi_i) + \rho\sin(\psi_i + \zeta_i) \end{cases} \tag{1.1}$$

where $\psi_i = \Omega t + \frac{2\pi(i-1)}{N_b}$ is the azimuth of the ith blade, with $i = 1, \ldots, N_b$. These expressions can be differentiated twice with respect to time, yielding

$$\begin{cases} \ddot{x}_i = \ddot{x}_h - e\Omega^2\cos(\psi_i) - \rho(\Omega + \dot{\zeta}_i)^2\cos(\psi_i + \zeta_i) - \rho\ddot{\zeta}_i\sin(\psi_i + \zeta_i) \\ \ddot{y}_i = \ddot{y}_h - e\Omega^2\sin(\psi_i) - \rho(\Omega + \dot{\zeta}_i)^2\sin(\psi_i + \zeta_i) - \rho\ddot{\zeta}_i\cos(\psi_i + \zeta_i) \end{cases} \tag{1.2}$$

Using D'Alembert's principle, the summation of moments about the lag hinge can be written as

$$\int \rho\sin(\psi_i + \zeta_i)\ddot{x}_i dm - \int \rho\cos(\psi_i + \zeta_i)\ddot{y}_i dm - c_i\dot{\zeta}_i - k_i\zeta_i = 0 \tag{1.3}$$

where the integrals are evaluated over the length of the blade $\int \rho dm = S_b$ and $\int \rho^2 dm = I_b$. thus obtaining the blade equations 1.11.

If the lead-lag is assumed to be small, such that $\cos\zeta_i \approx 1$ and $\sin\zeta_i \approx \zeta_i$, the equations become 1.9. This assumption is reasonable when the problem is asymptotically stable, because if the angle is too large the helicopter rotors cannot operate as intended. Nevertheless, in this thesis the nonlinear equations are studied without linearization, to show the potentiality of the method in cases where the nonlinearity cannot be neglected (i.e., elastomeric lag dampers).

If all blades in the rotor are assumed to have the same mass distribution, the coordinates for the center of mass of the entire rotor may be written as

$$\begin{cases} x_c = x_h + \frac{1}{N}\sum_{i=1}^{N} x_{i_c} \\ y_c = y_h + \frac{1}{N}\sum_{i=1}^{N} y_{i_c} \end{cases} \tag{1.4}$$

where x_{i_c} and y_{i_c} are the coordinates of the individual blade center of mass, measured

concerning the hub. They take the form

$$\begin{cases} x_{i_c} = e\cos(\psi_i) + \rho_{\text{cm}}\cos(\psi_i + \zeta_i) \\ y_{i_c} = e\sin(\psi_i) + \rho_{\text{cm}}\sin(\psi_i + \zeta_i) \end{cases} \tag{1.5}$$

with $\rho_{\text{cm}} = S_b/m_b$; the rotor center of mass coordinates become

$$\begin{cases} x_c = x_h - \frac{1}{N}\sum_{i=1}^{N}[e\cos(\psi_i) + \rho_{\text{cm}}\cos(\psi_i + \zeta_i)] \\ y_c = y_h + \frac{1}{N}\sum_{i=1}^{N}[e\sin(\psi_i) + \rho_{\text{cm}}\sin(\psi_i + \zeta_i)] \end{cases} \tag{1.6}$$

These expressions may now be differentiated twice in time

$$\begin{cases} P_x = -N_b m_b \ddot{x}_h - S_b\sum_{i=1}^{N}[\ddot{\zeta}_i\sin(\psi_i + \zeta_i) + (\Omega + \dot{\zeta}_i)^2\cos(\psi_i + \zeta_i) + \dfrac{e\Omega^2}{\rho}\cos\psi_i] \\ P_y = -N_b m_b \ddot{y}_h - S_b\sum_{i=1}^{N}[\ddot{\zeta}_i\cos(\psi_i + \zeta_i) - (\Omega + \dot{\zeta}_i)^2\sin(\psi_i + \zeta_i) - \dfrac{e\Omega^2}{\rho}\sin\psi_i] \end{cases} \tag{1.7}$$

Using D'Alembert's principle

$$\begin{cases} P_x = m_x\ddot{x}_h + c_x\dot{x}_h + k_x x_h \\ P_y = m_y\ddot{y}_h + c_y\dot{y}_h + k_y x_y \end{cases} \tag{1.8}$$

thus the hub equations, 1.12a and 1.12b, are obtained, where m_x and m_y represent the overall inertia of the airframe reduced to the respective hub displacement components, which can thus be different since one is related to the roll and the other to the pitch motion of the airframe. Similarly, c_x and c_y represent the damping of the airframe (mainly originating from the landing gear's shock absorbers) reduced to the corresponding components of hub motion, and k_x and k_y represent the stiffness of the airframe (also mainly related to the straining of the landing gear) reduced to the hub motion.

If lead-lag angles are assumed to be small, the hub equations 1.10a and 1.10b are obtained.

Number of blades, N_b	4
Blade mass, m_b	94.9 kg
Blade mass static moment, S_b	289.1 kg·m
Blade mass moment of inertia, I_b	1084.7 kg·m^2
Lag hinge offset, e	0.3048 m
Lag spring, k_i	0 m·N·rad^{-1}
Lag damper, c_i	4067.5 m·N·s·rad^{-1}
Hub mass, m_x	8026.6 kg
Hub mass, m_y	3283.6 kg
Hub spring, k_x	1240481.8 N·m^{-1}
Hub spring, k_y	1240481.8 N·m^{-1}
Hub damper, c_x	51078.7 N·s·m^{-1}
Hub damper, c_y	51078.7 N·s·m^{-1}

Table 1.1: Hammond model's data [13].

1.1.1. Linear, Time-Periodic Model

The equations of motion of Fig. 1.1, with the assumption of small Lead-Lag angles, thus are

$$\begin{aligned} &\ddot{\zeta}_i + \eta_i\dot{\zeta}_i + (\omega_{0i}^2 + \Omega^2\nu_0^2)\zeta_i \\ &- (\nu_0^2/e)[\ddot{x}_h \sin(\psi_i) - \ddot{y}_h \cos(\psi_i)] = 0 \quad i = 1 \dots N_b \end{aligned} \tag{1.9}$$

for each blade, with $\nu_0^2 = eS_b/I_b$, $\omega_{0i}^2 = k_i/I_b$, $\eta_i = c_i/I_b$.

The corresponding airframe equations of motion are

$$\begin{aligned} &(m_x + N_b m_b)\ddot{x}_h + c_x\dot{x}_h + k_x x_h \\ &- S_b \sum_{i=1}^{N_b}[(\ddot{\zeta}_i - \Omega^2\zeta_i)\sin(\psi_i) + 2\Omega\dot{\zeta}_i\cos(\psi_i)] = 0 \end{aligned} \tag{1.10a}$$

$$\begin{aligned} &(m_y + N_b m_b)\ddot{y}_h + c_y\dot{y}_h + k_y y_h \\ &- S_b \sum_{i=1}^{N_b}[(\ddot{\zeta}_i - \Omega^2\zeta_i)\cos(\psi_i) - 2\Omega\dot{\zeta}_i\sin(\psi_i)] = 0 \end{aligned} \tag{1.10b}$$

The numerical data proposed in [13] are reported in Table 1.1.

The usual approach for the analysis of the linearized equations consists in transforming the problem using multiblade coordinates, as originally proposed by Coleman [6]. The

blade equations are transformed into the non-rotating system of reference, eliminating the periodicity of the coefficients.

1.1.2. Nonlinear, Time-Periodic Model

The equations of motion of the system without the assumption of a small Lead-Lag angle (*ad-hoc* model), are thus

$$\begin{aligned} &I_b\ddot{\zeta}_i - f_i(\dot{\zeta}_i) + k_i\zeta_i + e\Omega^2 S_b \sin\zeta_i \\ &- S_b[\ddot{x}_h \sin(\psi_i + \zeta_i) - \ddot{y}_h \cos(\psi_i + \zeta_i)] = 0 \quad i = 1 \dots N_b \end{aligned} \tag{1.11}$$

for each blade, where $f_i(\dot{\zeta}_i)$ is the blade damping moment, with $f_i(\dot{\zeta}_i) = -c_i\dot{\zeta}_i$ when the linear damper of [13] is considered, and

$$\begin{aligned} &(m_x + N_b m_b)\ddot{x}_h + c_x\dot{x}_h + k_x x_h \\ &- S_b \sum_{i=1}^{N_b} [\ddot{\zeta}_i \sin(\psi_i + \zeta_i) + (\Omega + \dot{\zeta}_i)^2 \cos(\psi_i + \zeta_i) + \frac{e\Omega^2}{\rho_{\text{cm}}} \cos\psi_i] = 0 \end{aligned} \tag{1.12a}$$

$$\begin{aligned} &(m_y + N_b m_b)\ddot{y}_h + c_y\dot{y}_h + k_y y_h \\ &- S_b \sum_{i=1}^{N_b} [\ddot{\zeta}_i \cos(\psi_i + \zeta_i) - (\Omega + \dot{\zeta}_i)^2 \sin(\psi_i + \zeta_i) - \frac{e\Omega^2}{\rho_{\text{cm}}} \sin\psi_i] = 0 \end{aligned} \tag{1.12b}$$

for the airframe.

The numerical data are still those proposed in [13]; as anticipated, they are reported in Table 1.1. The difference between the linear and nonlinear systems is that when the solution is unstable, that of the linear system diverges. For the nonlinear one, instead, the solution can be divergent in the transitional region, but then reach an attractor or become chaotic. Thus, the study of the nonlinear model can give a clearer image of the type of instability, and suggest indications about how to reduce it. Also, the nonlinear equation follows the results obtained using multibody software, i.e., MBDyn (see Section 3.1), where no simplifying assumptions are made concering rigid body kinematics.

2 | Lyapunov Characteristic Exponents Theory and Application

Lyapunov Characteristic Exponents (LCEs) were introduced by Lyapunov [20] for the analysis of the stability of solutions of differential problems by the first approximation for regular time-varying linearizations, where the negativeness of the largest Lyapunov exponent indicated stability.

$$|\delta x(t)| \approx e^{\lambda t}|\delta x(t_0)| \tag{2.1}$$

While there are no general methods for checking the regularity of linearizations and there are known effects of the largest Lyapunov exponent sign inversions, called Perron effects [17], for nonregular time-varying linearizations, the computation of LCEs for linearization of the nonlinear autonomous system along nonstationary trajectories is widely used for the investigation of chaos, where the positiveness of the largest LCE is often considered as an indication of chaotic behavior in a nonlinear system.

As explained in [19], for ergodic systems LCEs are (nearly) independent of the trajectory $\vec{x}$ (the fiducial trajectory), as proved by Oseledec [28]. As such, they convey information about the global stability of the problem. Their definition involves the limit for $t \to \infty$; when computed from numerical integration, the computation of the solution $x_i(t)$ needs to stop at a finite time. The resulting value λ_i represents an estimate of the actual LCE. Whenever the problem evolves towards a stationary solution, the LCE estimates also converge to a finite value. According to the ellipsoid interpretation, a positive LCE indicates that the ellipsoid is growing along that direction in the state space; a negative LCE indicates contraction. Intuitively, expansion indicates instability, while contraction indicates stability (exponential stability): solutions originating from a perturbation along a direction associated with a positive LCE will depart from the original solution and vice versa. When the largest LCE is negative, the solution is exponentially stable about an equilibrium point in state space, an attractor of the problem. When the largest LCE is

zero, and all the others are negative, the attractor is a line in state space. Higher-order attractors (tori) occur when more than one LCE is zero. A positive LCE indicates chaotic behavior.

2.1. Floquet-Lyapunov Theory

The study of the stability of nonlinear, time-periodic systems is a well-known field where the theory was established by Gaston Floquet [11]. The following steps are extrapolated from the lecture on Floquet theory [24].

Let $\vec{x}^{(0)}(t)$, $\vec{x} \in \mathbb{R}^p$ collectively denote the solution in the p-dimensional phase space

$$\dot{\vec{x}} = \vec{f}(\vec{x}, t) \tag{2.2}$$

starting from some initial condition at time t_0 : $\vec{x}^{(0)}(t_0) = \vec{x}_0$. Consider now a different phase-trajectory $\vec{x}(t)$ starting at $t = t_0$ from a nearby point $\vec{x}_0 + \vec{w}_0$, and define $\vec{w}(t)$ to be the deviation vector $\vec{x}(t) - \vec{x}^{(0)}(t) = \vec{w}(t)$. In components, expanding the equation around the unperturbed trajectory thus obtaining

$$\begin{aligned} \dot{x}_i &= \cancel{\dot{x}_i^{(0)}} + \dot{w}_i = f_i(\vec{x}^{(0)}(t) + \vec{w}(t), t) \\ &= \cancel{f_i(\vec{x}^{(0)}(t), t)} + \sum_j \frac{\partial f_i}{\partial x_j}(\vec{x}^{(0)}(t), t) w_j(t) + \dots \end{aligned} \tag{2.3}$$

where the $\dots$ indicate higher-order terms in $\vec{w}$. Defining $\mathbf{J}(t)$ to be the Jacobian matrix

$$[\mathbf{J}]_{ij}(t) = \frac{\partial f_i}{\partial x_j}(\vec{x}^{(0)}(t), t) \tag{2.4}$$

and dropping higher-order terms, the linearized equations

$$\dot{\vec{w}}(t) = \mathbf{J}(t) \cdot \vec{w}(t) \tag{2.5}$$

are obtained. If the Jacobian matrix is time-periodic

$$\dot{\vec{w}}(t) = \mathbf{J} \cdot \vec{w} \quad \mathbf{J}(t + T) = \mathbf{J}(t), \tag{2.6}$$

where T is the period. This might occur in various circumstances, for instance when analyzing the stability of a time-periodic orbit $\vec{x}^{(0)}(t + T) = \vec{x}^{(0)}(t)$ of an autonomous system, where the system itself $\vec{f}(\vec{x})$ does not depend on time explicitly, this includes, for

instance, a limit cycle in a dissipative system.

The p linearly independent solutions of the linear time-periodic problem can always be written as a product of a time-periodic part $\vec{u}_j(t)$ times a pure "exponential term" $e^{\lambda_j(t-t_0)}$

$$\vec{w}_j(t) = e^{\lambda_j(t-t_0)}\vec{u}_j(t) \quad \vec{u}_j(t+T) = \vec{u}_j(t) \tag{2.7}$$

The eigenvalues λ_j j can be deduced by studying the propagator over one period. They play a crucial role, since if $Re\lambda_j > 0$ the linear system will be unstable. The one-period propagator $\mathbf{L}_0 = \mathbf{L}(t_0+T, t)$, which can be obtained by integrating the matrix version of the flow equation 2.5, in general numerically, starting from initial condition $\mathbf{W}(t_0) = \mathbb{I}$, where $\mathbf{W} = [\vec{w}_1, ..., \vec{w}_p]$.

$$\mathbf{W}(t_0+T) = \mathbf{L}(t_0+T, t_0)\mathbf{W}(t_0) = \mathbf{L}(t_0+T, t_0) \tag{2.8}$$

Assume that $\mathbf{L}(t_0+T, t_0)$ can be diagonalized. It means that p eigenvectors exist; denote them by $\vec{u}_j(t_0)$, such that

$$\mathbf{L}_0 \cdot \vec{u}_j(t_0) = \mu_j\vec{u}_j(t_0) \quad with \quad j = 1, ..., p \tag{2.9}$$

where $\mu_j \in \mathbb{C}$ are known as Floquet modes. The eigenvalues μ_j are related to the λ_j as follows

$$\lambda_j = \frac{1}{T}\log(\mu_j) \tag{2.10}$$

where the principal value of the imaginary part (although irrelevant in this study) is considered. Hence, the stability of the linear problem requires

$$\forall j \quad |\mu_j| \leq 1 \quad \Longleftrightarrow \quad \mathrm{Re}\,\lambda_j \leq 0 \tag{2.11}$$

2.2. Lyapunov Characteristic Exponents

In the case of a complex dynamical system, the Jacobian matrix $\mathbf{J}$ usually is time-dependent, so the stability cannot be analyzed in terms of eigenvalues of $\mathbf{J}$. For this reason, one approach is to use the Lyapunov Characteristic Exponent. Consider the dynamical system defined on a differentiable manifold S. Let $\phi^t(\vec{x})$ denote the state at time t of the system which at time $t = 0$ was at $\vec{x}$. For the action of ϕ^t over two successive

time intervals t and s we have the following composition law

$$\phi^{t+s} = \phi^t \circ \phi^s \tag{2.12}$$

The deviation vector $\vec{w}$ evolve on the tangent space T_xS of S. The $d_{\vec{x}}\phi^t$ is the linear mapping which maps the tangent space of S at point $\vec{x}$ onto the tangent space at point $\phi^t(\vec{x})$ thus $d_{\vec{x}}\phi^t : T_xS \to T_{\phi^t(\vec{x})}S$ with

$$\vec{w}(t) = d_{\vec{x}}\phi^t \cdot \vec{w}(t_0) \tag{2.13}$$

The tangent space at x is mapped onto the tangent space at $\phi^t(\vec{x})$ by the differential $d_{\vec{x}}\phi^t$. Thus, the action of $d_{\vec{x}}\phi^t$ on a particular initial deviation vector $\vec{w}$ of the tangent space is given by the multiplication of matrix $\mathbf{Y}(t, t_0)$ (State Transition Matrix) in terms of which the solution of 2.5 can be written as

$$\vec{w}(t) = \mathbf{Y}(t, t_0) \cdot \vec{w}(t_0) \tag{2.14}$$

From the Oseledec Multiplicative Ergodic Theorem [21] (explained in Appendix B) states that the following limit exists

$$\Lambda^{\pm}(t) = \lim_{t\to\pm\infty} \frac{1}{2t} \log([\mathbf{Y}^{\dagger}(t, t_0)\mathbf{Y}(t, t_0)]) \tag{2.15}$$

or can be written in the following form (explained in Appendix B)

$$\lambda_i = \lim_{t\to\infty} \frac{1}{t} \log\left(\frac{||\mathbf{Y}(t, t_0) \cdot \vec{w}_i(t_0)||}{||\vec{w}_i(t_0)||}\right) \tag{2.16}$$

where $||..||$ indicates a smooth Riemannian metric. A more complete insight of LCEs is given by Charalampos Skokos [25].

2.3. LCEs Estimation Using the Discrete QR Method

A typical approach for computing all LCEs consists of evaluating the evolution of the discrete QR factorization [1]. One of the most popular methods for the estimation of LCEs [19], it is based on incrementally updating the LCE estimates with the diagonal elements of the upper-triangular matrix $\mathbf{R}$ obtained from the QR factorization of the incremental

state transition matrix, $\mathbf{Y}(t_k, t_{k-1})$, between two consecutive time steps. Consider

$$\vec{w}_i(t_k) = (\mathbf{Y}(t_k, t_{k-1})\mathbf{Y}(t_{k-1}, t_{k-2}) \dots \mathbf{Y}(t_1, t_0)) \cdot \vec{w}_i(t_0) \tag{2.17}$$

$$\vec{w}_i(t_k) = \prod_{k=1}^{n} \mathbf{Y}(t_k, t_{k-1}) \cdot \vec{w}_i(t_0) \tag{2.18}$$

this can be rewritten into $\mathbf{W} = [\vec{w}_1, ..., \vec{w}_p]$

$$\mathbf{W}(t_k) = \prod_{k=1}^{n} \mathbf{Y}(t_k, t_{k-1})\mathbf{W}(t_0) \tag{2.19}$$

at this point the discrete QR is applied

$$\mathbf{W}(t_k) = \mathbf{Q}(t_k)\mathbf{R}(t_k) \tag{2.20}$$

$$\mathbf{Q}(t_k)\mathbf{R}(t_k) = \prod_{k=1}^{n} \mathbf{Y}(t_k, t_{k-1})\mathbf{Q}(t_0) \tag{2.21}$$

one can notice that

$$\mathbf{Y}(t_k, t_{k-1})\mathbf{Q}(t_{k-1}) \prod_{s=0}^{k-1} \mathbf{R}(t_{k-s}) = \tag{2.22}$$
$$\mathbf{Q}(t_k)\mathbf{R}(t_k) \prod_{s=0}^{k-1} \mathbf{R}(t_{k-s}) = \mathbf{Q}(t_k) \prod_{s=0}^{k} \mathbf{R}(t_{k-s})$$

This way, $\mathbf{Y}(t_k, t_{k-1})\mathbf{Q}(t_{k-1}) \prod_{s=0}^{k-1} \mathbf{R}(t_{k-s})$ can be used to construct the QR factorization of the State Transition Matrix from t_0 to t_k as $\mathbf{Y}(t_k, t_0) = \mathbf{Q}(t_k) \prod_{s=0}^{k} \mathbf{R}(t_{k-s})$ by only considering incremental QR factorizations over $\mathbf{Y}(t_k, t_{k-1})\mathbf{Q}(t_{k-1})$, i.e., with limited contraction/expansion in each matrix $\mathbf{R}(t_k)$. by taking the definition of LCEs 2.16 and by substituting with the deviation vectors obtained in equation

$$\lambda_i = \lim_{t \to \infty} \frac{1}{t} \log \left(\frac{||\vec{w}_i(t)||}{||\vec{w}_i(t_0)||} \right) \tag{2.23}$$

for a discrete time system:

$$\lambda_i = \lim_{n \to \infty} \frac{1}{n\Delta t} \log \left(\prod_{k=1}^{n} \frac{||\vec{w}_i(t_k)||}{||\vec{w}_i(t_{k-1})||} \right) \tag{2.24}$$

$$\lambda_i = \lim_{n\to\infty} \frac{1}{n\Delta t} \sum_{k=1}^{n} \log\left(\frac{||\vec{w}_i(t_k)||}{||\vec{w}_i(t_{k-1})||}\right) \tag{2.25}$$

By using the QR factorization, the value of $||\vec{w}_j(t_k)||/||\vec{w}_j(t_{k-1})||$ corresponds to the diagonal elements of matrix $\mathbf{R}(t_k)$, so $r_{ii}(t_k) = \gamma_{ik}$. In the Gram-Schmidt orthonormalization method, the matrix $\mathbf{Q}$ stores the local basis and the matrix $\mathbf{R}$, in the diagonal part, stores the stretch in the principal local direction, and, in the strictly upper triangular part, the projection of the stretch in the other principal axes.

$$\vec{w}_i(t_k) = \sum_{j=1}^{i-1} \langle \hat{\vec{w}}_j(t_k), \vec{w}_i(t_k)\rangle \hat{\vec{w}}_j(t_k) + \gamma_{ik}\hat{\vec{w}}_i(t_k) \quad i = 1\dots p \tag{2.26}$$

For the estimation of the LCEs, only the stretch in the principal directions are needed, Thus yielding:

$$\lambda_i = \lim_{n\to\infty} \frac{1}{n\Delta t} \log\left(\prod_{k=1}^{n} \gamma_{ik}\right) \tag{2.27}$$

can be incrementally computed as a sum which helps prevent overflow or underflow in numerical computations, leading to

$$\lambda_i = \lim_{n\to\infty} \frac{1}{n\Delta t} \sum_{k=1}^{n} \log(\gamma_{ik}) \tag{2.28}$$

2.4. LCEs Jacobianless Method

In many applications, the Jacobian matrix cannot be extracted because the system is unknown or is too complex to evaluate the Jacobian matrix in analytical form. In this case, two approaches can be used. The first is to numerically evaluate the Jacobian matrix, when the system can be evaluated at an arbitrary state and time (see Section 2.4.1). The second is to use directly the time series of the solution to estimaate the maximum LCE (2.4.2). In the present work, the MLCE approach is considered for its simplicity and also because it can be easily implemented using existing software (for example with *MBDyn*, as discussed in Section 3.1)

2.4.1. Numerical Jacobian Approximation Method

One method to approximate the Jacobian matrix is to estimate it by numerical approximation. By using the algorithm proposed by Dieci [10], all the LCEs of a problem can be estimated without the knowledge of the Jacobian matrix; however, this method still

requires the possibility to evaluate the problem for an arbitrary status and time. This is not always possible, so other methods (e.g., Section 2.4.2) need to be used. This method is detailed in Appendix A.

2.4.2. Maximum LCE Method

In most applications, estimating the Maximal LCE may suffice. The algorithm proposed by Rosenstein [23] is able to estimate the MLCE from a short time series. From a time series the trajectory, $\mathbf{X}$, can be reconstructed using the time delay method. The reconstructed trajectory can be expressed as a matrix where each row is a phase-space vector. That is,

$$\mathbf{X} = [\mathbf{X}_1, \mathbf{X}_2, ..., \mathbf{X}_m] \tag{2.29}$$

For an N-point time series, $\{x_1, x_2, ..., x_N\}$, each $\mathbf{X}_k$ is given by

$$\mathbf{X}_k = [x_{1+(k-1)J}, x_{2+(k-1)J}, ..., x_{M+(k-1)J}]^T \tag{2.30}$$

where $k = 1, ..., m$.
Thus, $\mathbf{X}$ is an $M \times m$ matrix, and the constants m, M, J, and N are related as

$$M = N - (m-1)J \tag{2.31}$$

where m is the embedding dimension, N the length of the time series, and J the reconstruction delay. The embedding dimension is usually estimated in accordance with Takens' theorem, i.e., $m > 2n$.

After reconstructing the dynamics, the algorithm locates the nearest neighbor of each point on the trajectory. The nearest neighbor, $\mathbf{X}_{\hat{j}}$, is found by searching for the point that minimizes the distance to the particular reference point, $\mathbf{X}_j$. This is expressed as

$$d_j(0) = \min_{\mathbf{X}_{\hat{j}}} ||\mathbf{X}_j - \mathbf{X}_{\hat{j}}|| \tag{2.32}$$

where $d_j(0)$ is the initial distance from the j^{th} point to its nearest neighbor, and $||..||$ denotes the Euclidean norm. Also, an additional constraint is that nearest neighbors have a temporal separation greater than the mean period ($\bar{T}$) (the reciprocal of the mean frequency of the power spectrum, although it can be expected that any comparable estimate, e.g., using the median frequency of the magnitude spectrum, yields equivalent results) of

the time series

$$|j - \hat{j}| > \bar{T} \tag{2.33}$$

This allows considering each pair of neighbors as nearby initial conditions for different trajectories. The largest Lyapunov exponent is then estimated as the mean rate of separation of the nearest neighbors.

The j^{th} pair of nearest neighbors diverge approximately at a rate given by the largest Lyapunov exponent:

$$d_j(i) \approx C_j e^{\lambda_1 (i\Delta t)} \tag{2.34}$$

where C_j is the initial separation.

By taking the logarithm of both sides

$$\ln d_j(i) \approx \ln C_j + \lambda_1 (i\Delta t) \tag{2.35}$$

a set of approximately parallel lines (for $j = 1, 2, ..., M$) is obtained, each with a slope roughly proportional to λ_1. The largest Lyapunov exponent is calculated using a least-squares fit to the "average" line defined by

$$y(i) = \frac{1}{\Delta t} \langle \ln d_j(i) \rangle \tag{2.36}$$

where $\langle .. \rangle$ denotes the average over all values of j.

A disadvantage of this method is that estimating some parameters, e.g., the embedding dimension or the mean frequency, can be difficult. Another problem arises when multiple time series are extracted, which one to choose for the reconstruction of the trajectory by the time delay method (the reconstruction of the trajectory is not necessary in this case because all time series of the system are available). The time series can be chosen in different multiple ways, i.e., by using the principal orthogonal decomposition. After the time series is reconstructed, a random permutation is applied (this is to improve the calculation of the mean; it is possible to use all the values of the time series, but then the computational cost increases). Then the first constraint is applied by checking if the distance from the reference point is less than the mean period for a given reference point; in that case, the reference distance is calculated by finding the minimum of all distances from the reference point. This process is repeated for each random permutation. Then the distances for each random permutation are evolved, and, for each step, the mean is calculated with all the random permutations. Then, after the evolution in time with the logarithm of the distance vector multiplied by the sampling frequency, a linear fit is made.

From the linear interpolation, the slope represents the MLCE.

2.5. LCEs of the Hammond Model

2.5.1. Linear, Time-Periodic Model

To study the stability of the Linear, Time-Periodic model, Floquet's theory (Section 2.1) is used. The first case, with all Lead-Lag dampers operative (isotropic case), is presented in Fig. 2.1. The second case, with one Lead-Lag damper inoperative (non-isotropic case) is presented in Fig. 2.2. This study was presented by [13] to understand the instability of the ground resonance model; the results in the plots are in perfect agreement with those of Hammond.

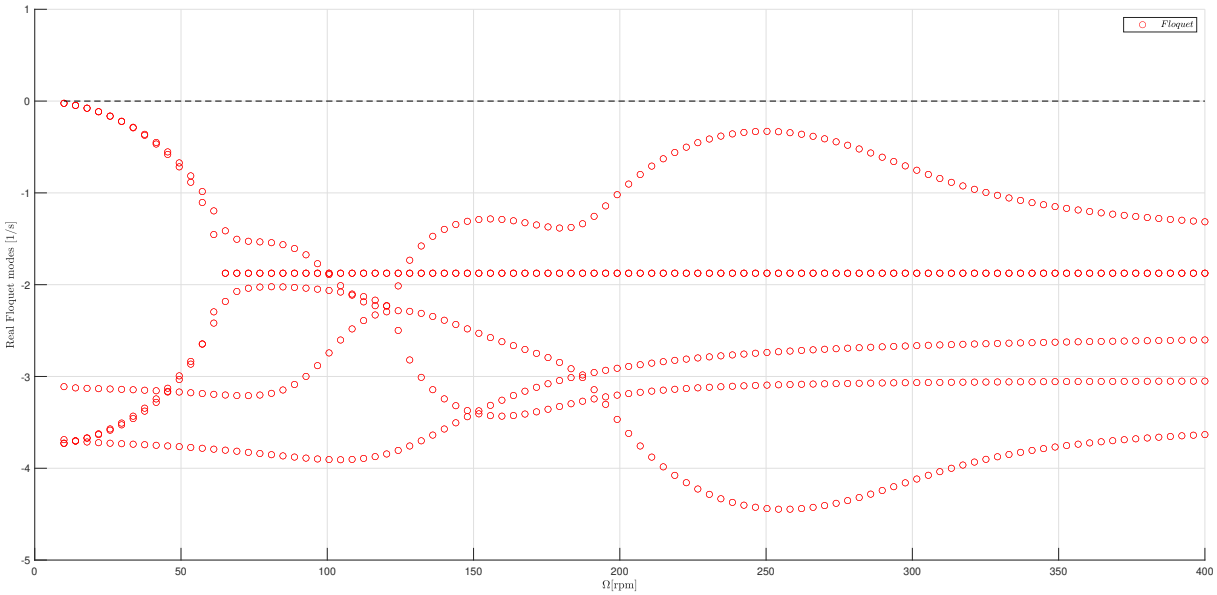

Figure 2.1: Real Floquet modes of the isotropic case.

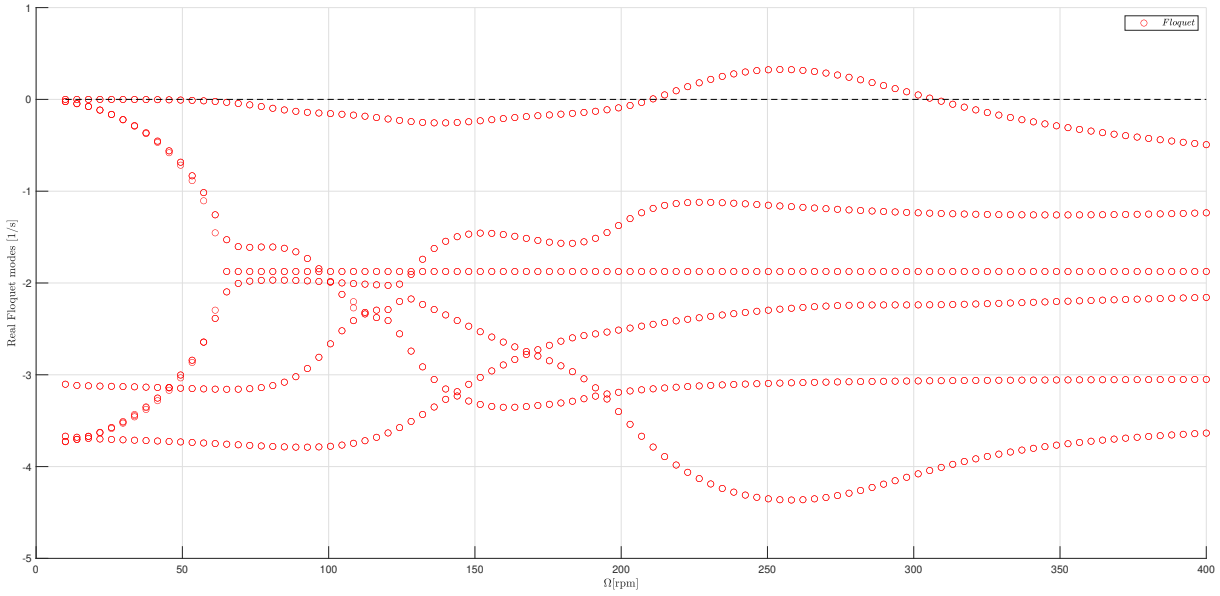

Figure 2.2: Real Floquet modes of the non-isotropic case.

2.5.2. Nonlinear, Time-Periodic Model

To study the stability of the Nonlinear, Time-Periodic model, the LCEs approach (Section 2.3) is used. The first case, with all Lead-Lag Dampers operative, is presented in Fig. 2.3. The second case, with one Lead-Lag Damper inoperative (the third Lead-Lag Damper), is presented in Fig. 2.4. As expected, the first case with all Lead-Lag Dampers operative converges to the one obtained by Hammond [13]. In the second case, a different result is obtained in the instability region: the LCEs show that the solution after a transient region of divergence converges to a stable limit cycle; in fact, the first LCE converges to zero.

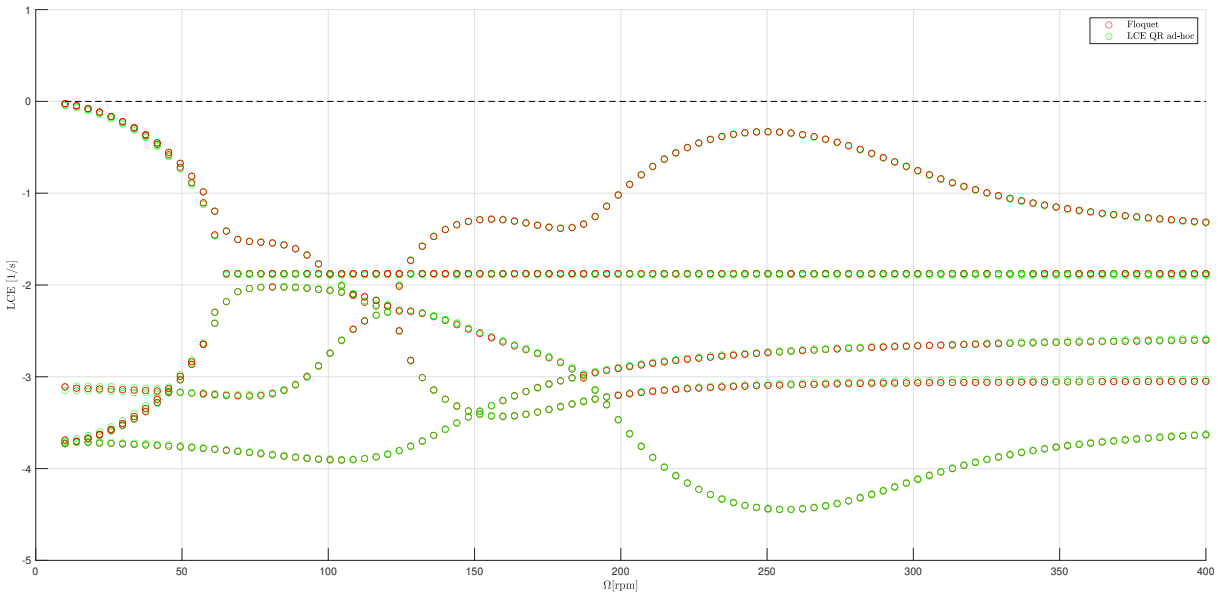

Figure 2.3: LCEs of the isotropic case.

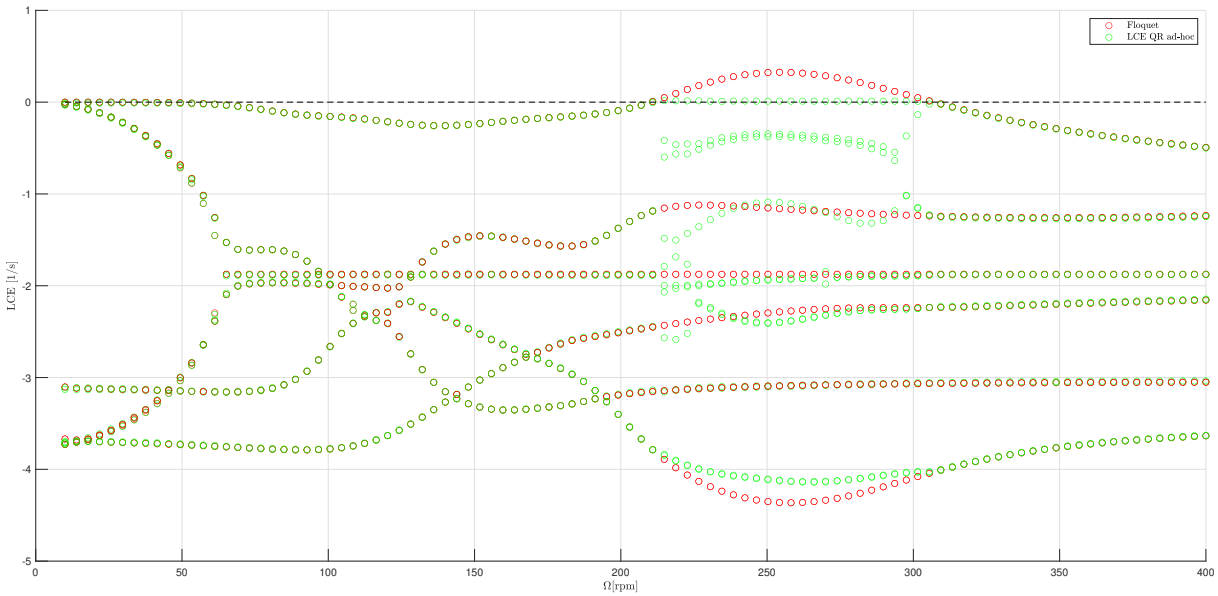

Figure 2.4: LCEs of the non-isotropic case.

The LCEs spectrum is local and depends on the initial value of the system's solution. For all the calculations presented so far, an initial value of $x_0 = 0.1$ m is used. Figure 2.4 shows that, as expected, the instability region is the same as that of the Linear, Time-Periodic model with the only difference that the solution is not unstable but, after a transient, converges to a stable limit cycle.

3 | LCEs and Multibody Analysis

3.1. MLCE of the MBDyn Model

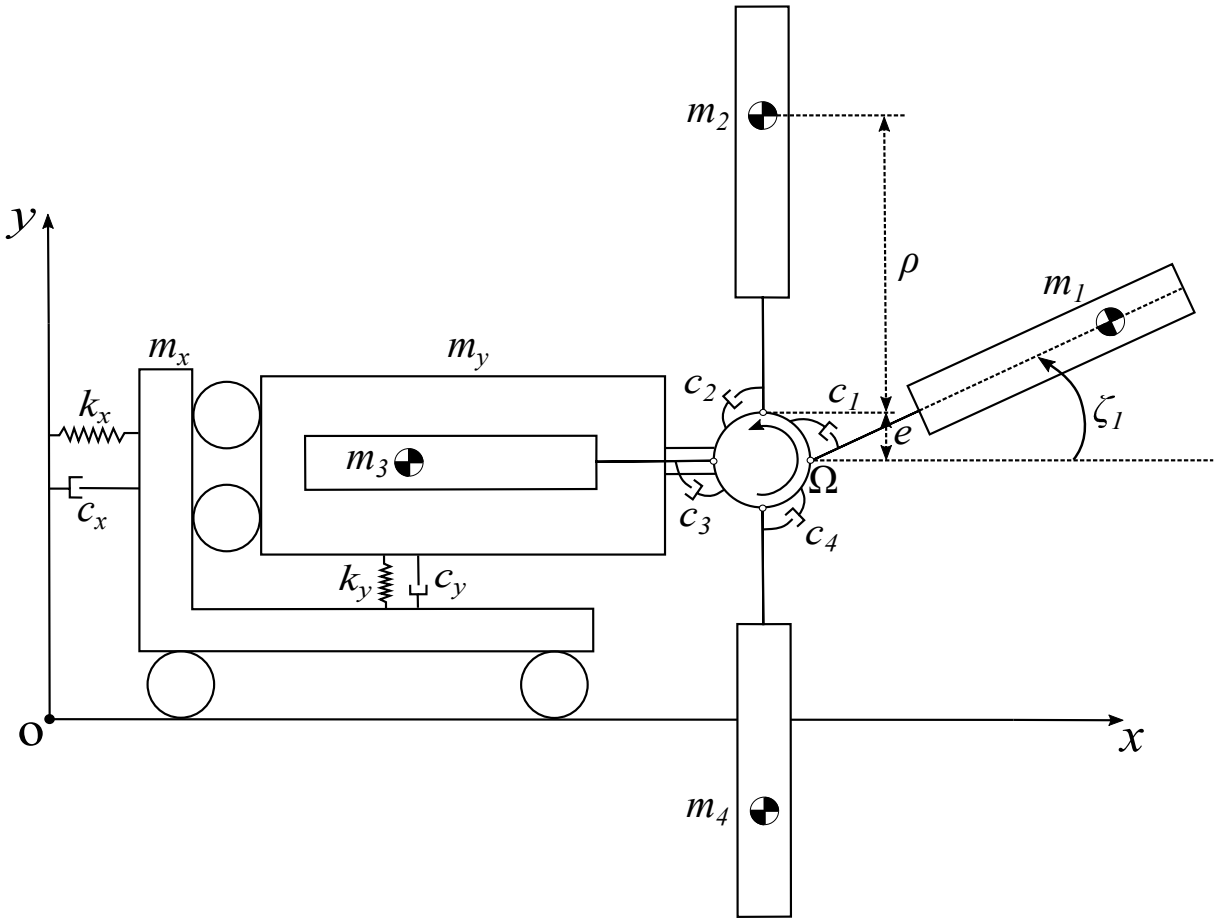

Figure 3.1: Sketch of the MBDyn model of Hammond's system [13].

One application of the Maximum LCE method (2.4.2) is to study the stability/instability of complex and short time series. By using MBDyn, it is possible to obtain the time evolution of a more complex model with more details regarding the ground resonance. To validate the method, the Hammond model is recreated using the MBDyn environment. However, owing to the peculiar modeling characteristics of the solver, the different equiv-

alent inertia terms of the airframe respectively associated with motion in the x and y directions had to be obtained by splitting the airframe into two parts:

- the first part is connected to the ground by a constraint that only allows its absolute displacement in the x direction;
- the second part is connected to the first one by a constraint that only allows its displacement relative to the first one in the y direction.

The mass of the second part is m_y, whereas that of the first one is $m_x - m_y$, such that the overall mass associated with the absolute motion of the hub center in the x direction corresponds to m_x.

The first part is connected to the ground by a spring and a damper, of characteristics k_x and c_x. Another spring and damper, of characteristics k_y and c_y, connect the second to the first part.

The rotor hub is modeled as a third, massless part, whose relative motion with respect to the second part of the airframe is a prescribed rotation about axis z with constant rpm.

The blades are described as rigid bodies through their absolute displacement and orientation, constrained to the hub by revolute joints that only allow their relative rotation about the lead-lag hinge, whose axis is parallel to the global z axis, and thus to the axis of rotation of the rotor. Such rotation is restrained by an angular damper that represents the equivalent lead-lag damper torque.

A sketch of the model is shown in Fig. 3.1. The MBDyn model of Hammond's problem is available from the project's website[1].

[1] `https://gitlab.com/zanoni-mbdyn/mbdyn-tests-public/-/tree/develop/Hammond/GR_MBDyn`

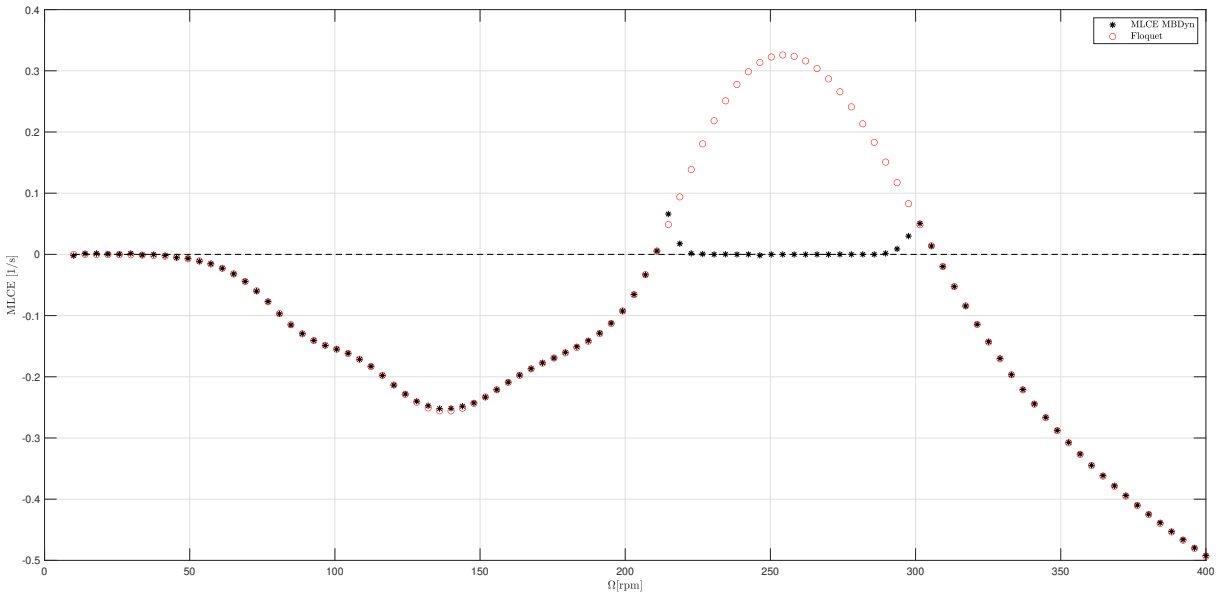

Figure 3.2: estimated MLCE of non-isotropic case, using Jacobian-less method.

The results of Fig. 3.2 show that with the MLCE method it is possible to obtain the maximum LCE and thus to evaluate the stability/instability of the system. The results follow those obtained in Section 2.5. For comparison, Fig. 3.4 for the non-isotropic case with one damper inoperative and Fig. 3.3 for the isotropic case are reported. As expected, for the non-isotropic case the MLCE follows the maximum exponent of the results obtained in Section 2.5.2.

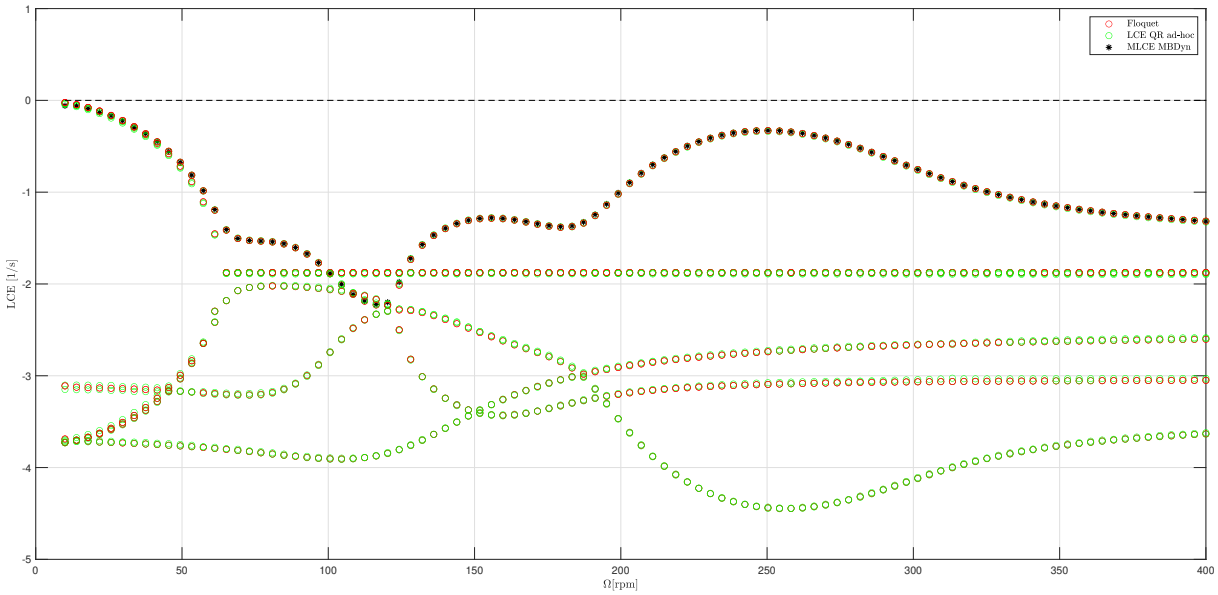

Figure 3.3: LCEs of the isotropic case.

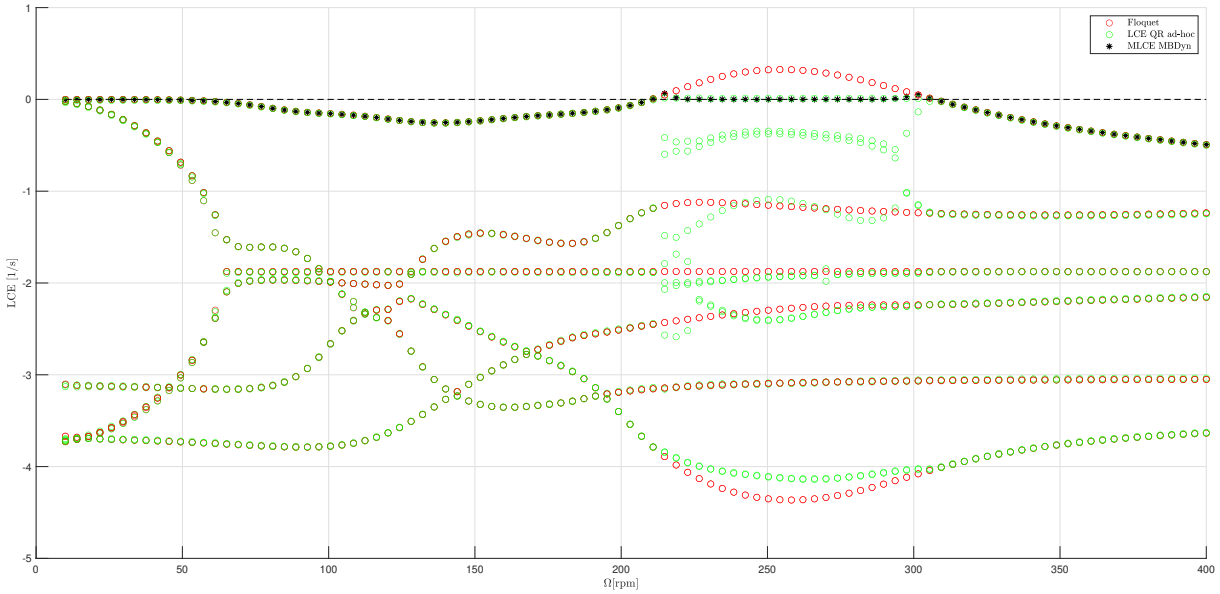

Figure 3.4: LCEs of the non-isotropic case.

The phase space can be useful to visualize the difference between stability and instability. From Fig. 3.5, two case are extrapolated. In the first case, $\Omega = 124.2$ rpm, a negative MLCE shows that the solution is stable; indeed, the phase space of Fig. 3.6 converges to the point of stability. In the second case, $\Omega = 242.4$ rpm, a(a almost) zero MLCE shows that the solution converges to a limit cycle; the phase-space of Fig. 3.7 shows that the solution is a stable orbit.

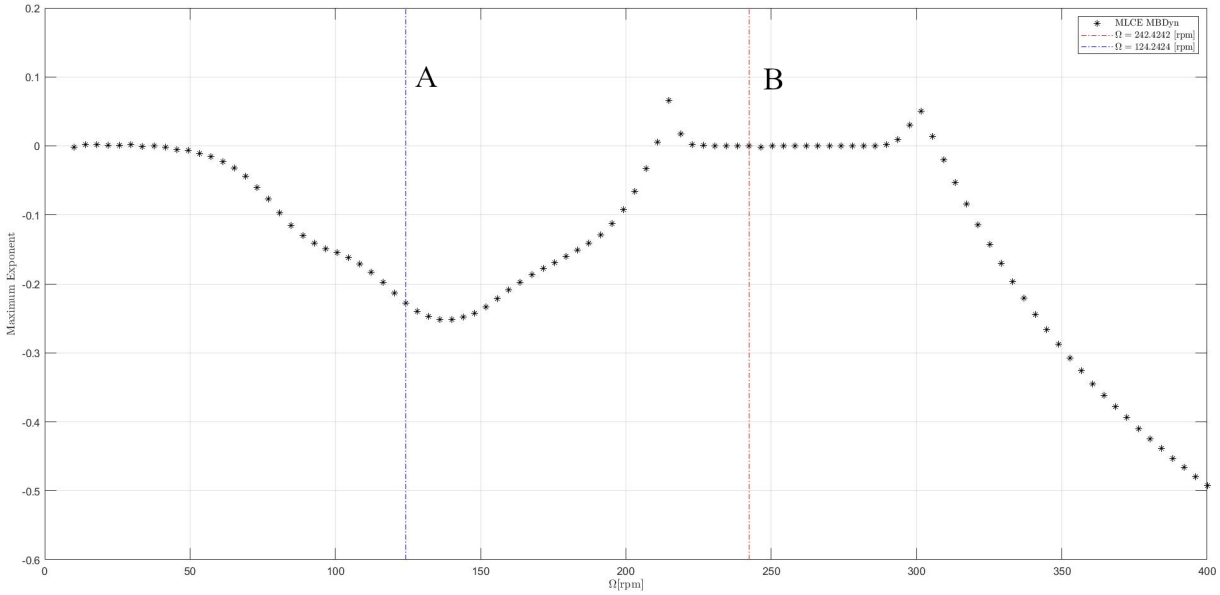

Figure 3.5: MLCE of non-isotropic case, using Jacobian-less method.

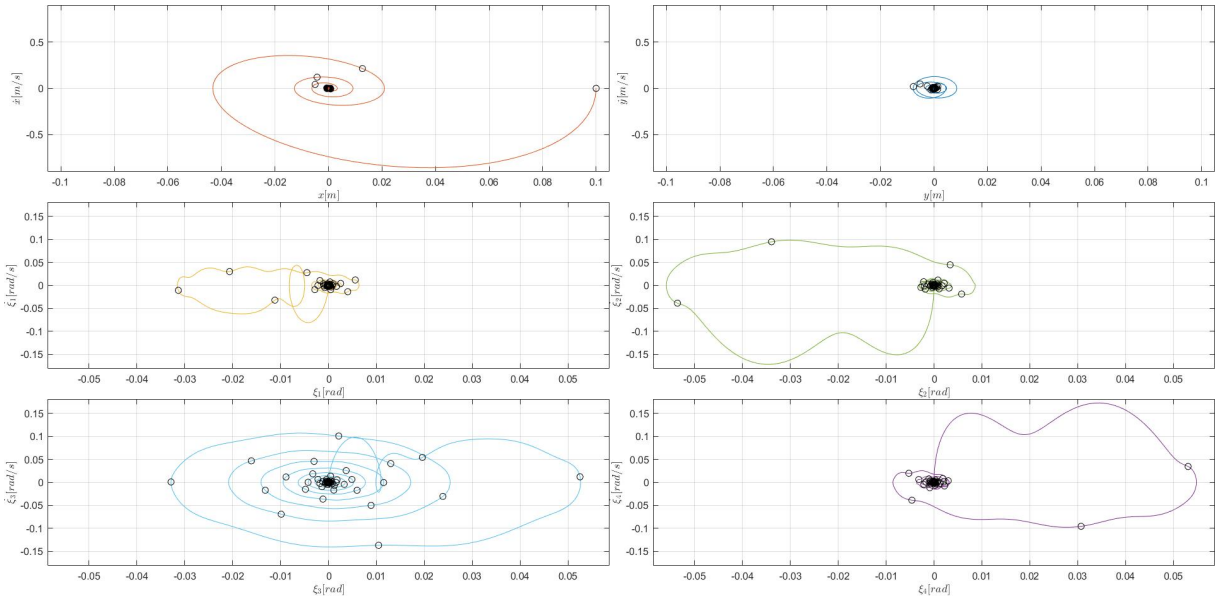

Figure 3.6: Case A: phase space at $\Omega = 124.2$ rpm.

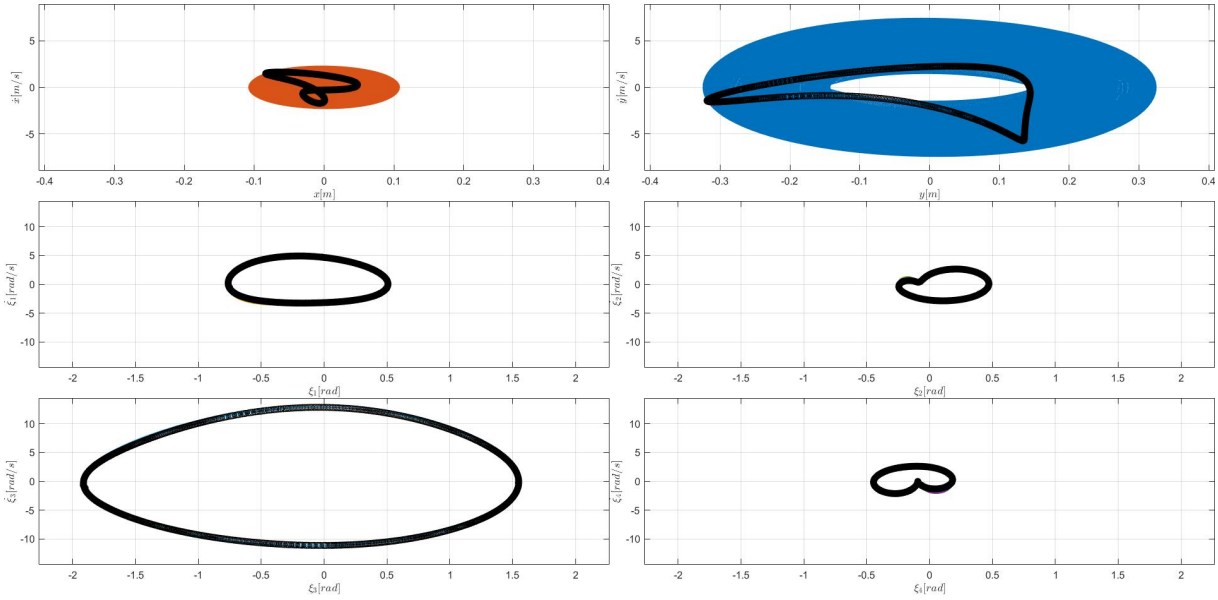

Figure 3.7: Case B: phase space at $\Omega = 242.4$ rpm.

One aspect of the MLCE method is that it requires the time series to be in the attractor region to give an accurate value. In Fig. 3.8, near $\Omega = 220$ rpm and $\Omega = 300$ rpm the MLCE value is not exactly zero. This is due to the fact that the transitional region is much longer, since the MLCE in the transitional region is slightly greater than zero and the growth of the solution is quite slow, so in the overall estimated MLCE there is also the contribution of the expansion of the transitional region. This effect can be mitigated by

using longer time series or by taking only the values after the system reaches the attractor region. This can also be used to estimate the expansion/contraction in the transitional region; the method is easier to implement for time series and for this reason can be useful to identify how the transitional region behaves.

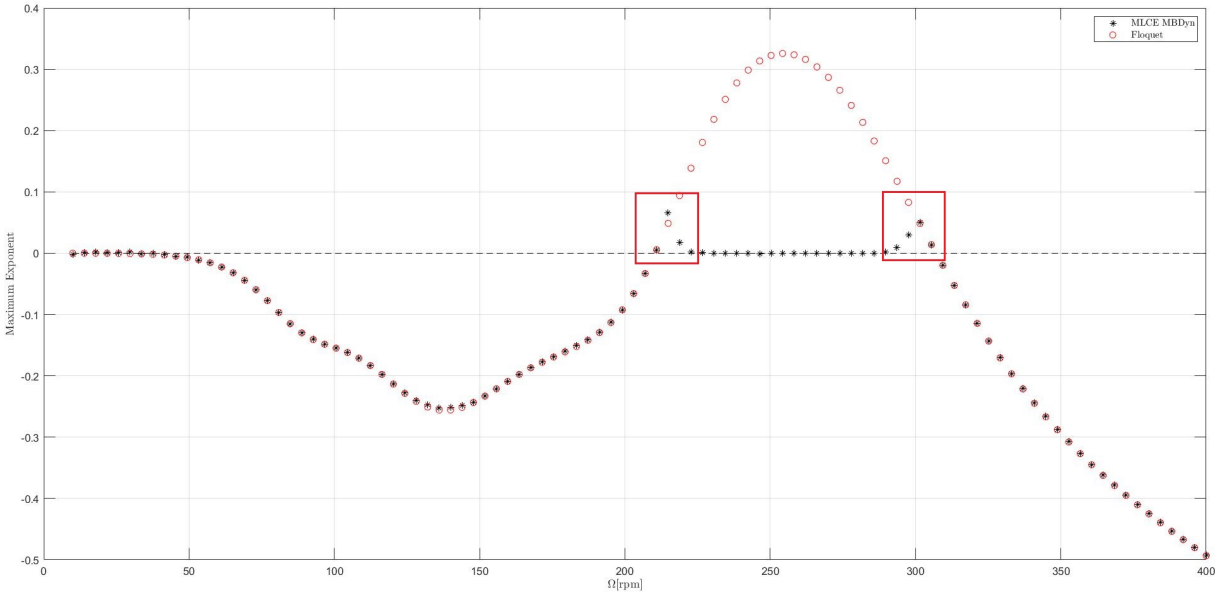

Figure 3.8: MLCE of the MBDyn model; red boxes represents the region where convergence is not reached.

3.2. Hammond Model with Nonlinear Dampers

The case of a more realistic damper model, characterized by the nonlinear constitutive law studied in [27], is considered. Even if the Hammond model gives an estimation of the instability region, a more details model is necessary to improve the understanding of the instability phenomenon. Another way to describe the nonlinearity of the constitutive law of the dampers is using polynomials that approximate their constitutive behavior, i.e., elastomeric dampers and the hub. This approach was used by Kunz [21]. The equations of motion of the *ad-hoc* system in the x hub direction (1.12a) and y hub direction (1.12b) remain unchanged. The main difference is the nonlinear law imposed on the dampers with saturation if the norm of the angular velocity exceeds a threshold. Thus, the blades equation is as follows

$$I_b\ddot{\xi}_i + f_{di} + k_i\xi_i + e\Omega^2 S_b sin(\xi_i) \tag{3.1}$$

$$- S_b[\ddot{x}_h \sin(\psi_i + \xi_i) - \ddot{y}_h \cos(\psi_i + \xi_i)] = 0 \quad i = 1, ..., N \tag{3.2}$$

where

$$f_{di} = \begin{cases} \chi\dot{\xi}_i|\dot{\xi}_i| + C_L\dot{\xi}_i & |\dot{\xi}_i| < |\dot{\xi}_L| \\ \bar{\chi}\dot{\xi}_L|\dot{\xi}_L| & |\dot{\xi}_i| \geq |\dot{\xi}_L| \end{cases} \tag{3.3}$$

with $\chi = \bar{\chi} - C_L\dot{\xi}_L$ and $\bar{\chi} = 1.2203 \times 10^6$ N·m·s^2/rad^2, $\dot{\xi}_L = 1.0$ deg/s, $C_L = c_i$.

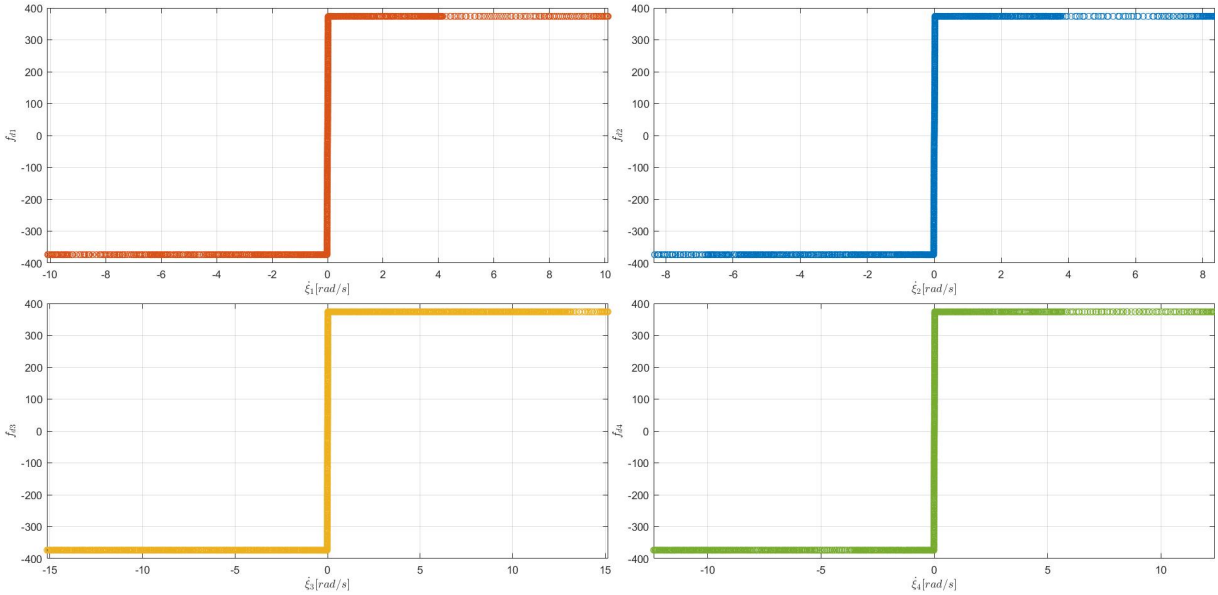

Figure 3.9: Lead-Lag dampers with saturation.

3.2.1. All Lead-Lag Dampers Operative

In the first case study, all the Lead-Lag dampers are operative. The initial angular velocity of the third blade is varied, to trigger the saturation that occurs in the damper's constitutive law when the norm of the angular velocity exceeds the given threshold. The solution reaches a limit cycle if the initial angular velocity is greater than the saturation threshold, and ground resonance becomes possible even when all dampers are operative.

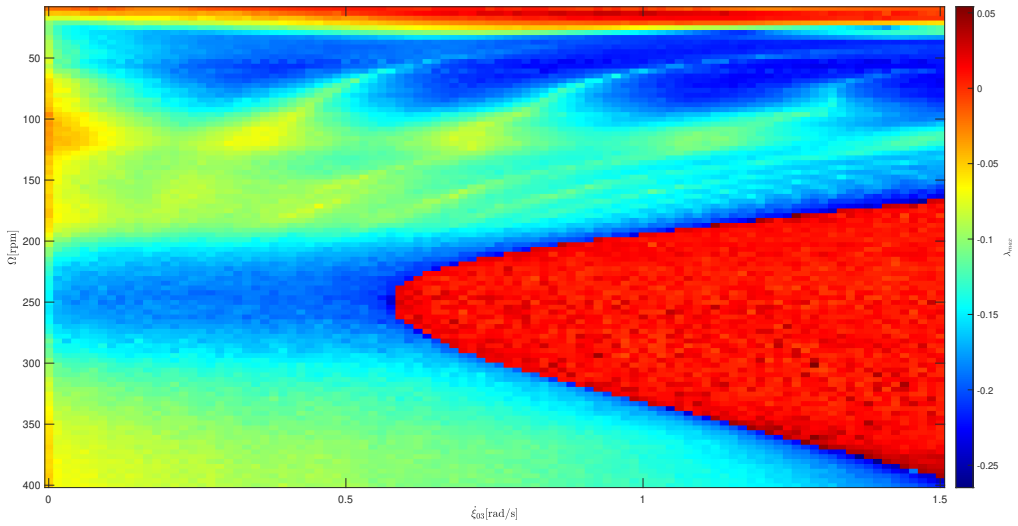

Figure 3.10: MLCE with different initial angular velocity of $\dot{\xi}_{03}$.

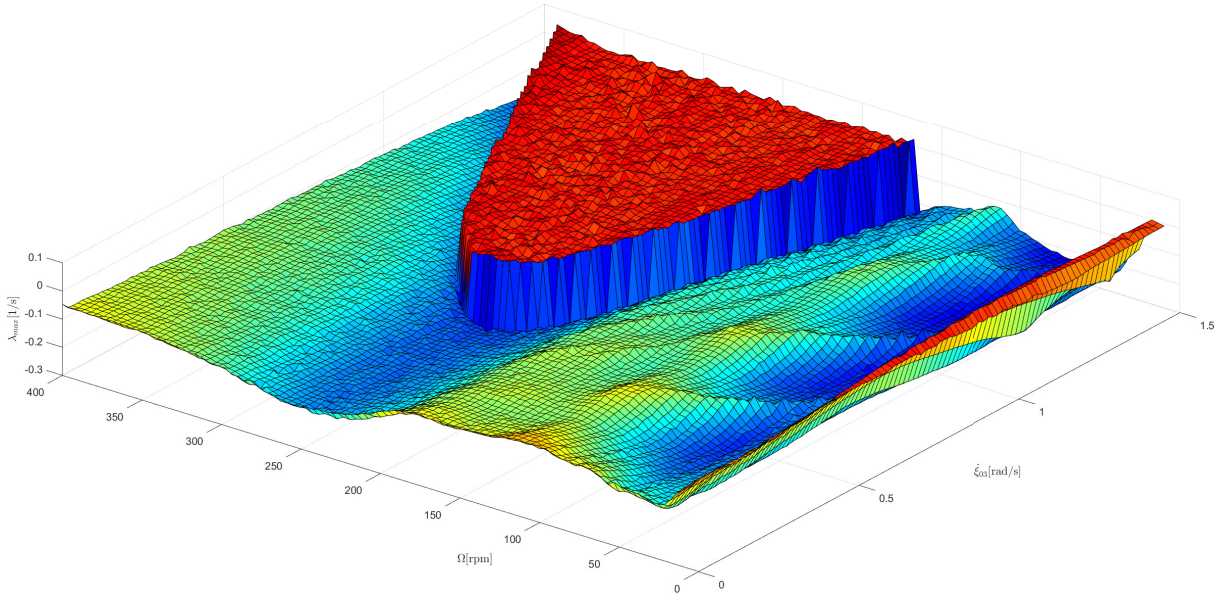

Figure 3.11: 3D plot of the MLCE with different initial angular velocity of $\dot{\xi}_{03}$.

3.2.2. One Lead-Lag Damper Inoperative

In this case study, the third Lead-Lag damper is inoperative. Different initial angular velocities are considered for this blade. The solution reaches a limit cycle and the range of angular velocities with this limit-cycle solution increases with the value of the initial angular velocity. This also shows the locality of the LCEs: it means that the solutions depend on the initial condition, as expected.

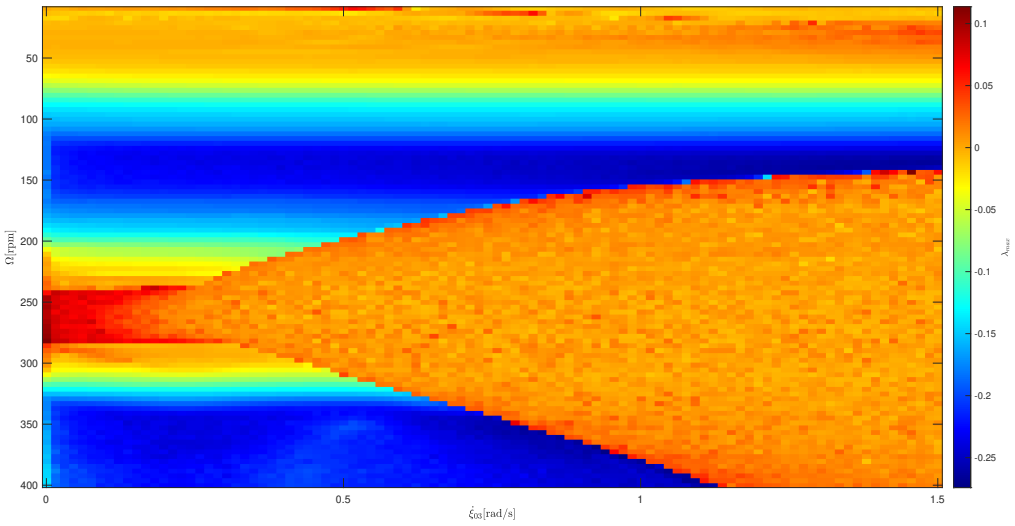

Figure 3.12: MLCE with the third damper inoperative and different initial condition of $\dot{\xi}_{03}$.

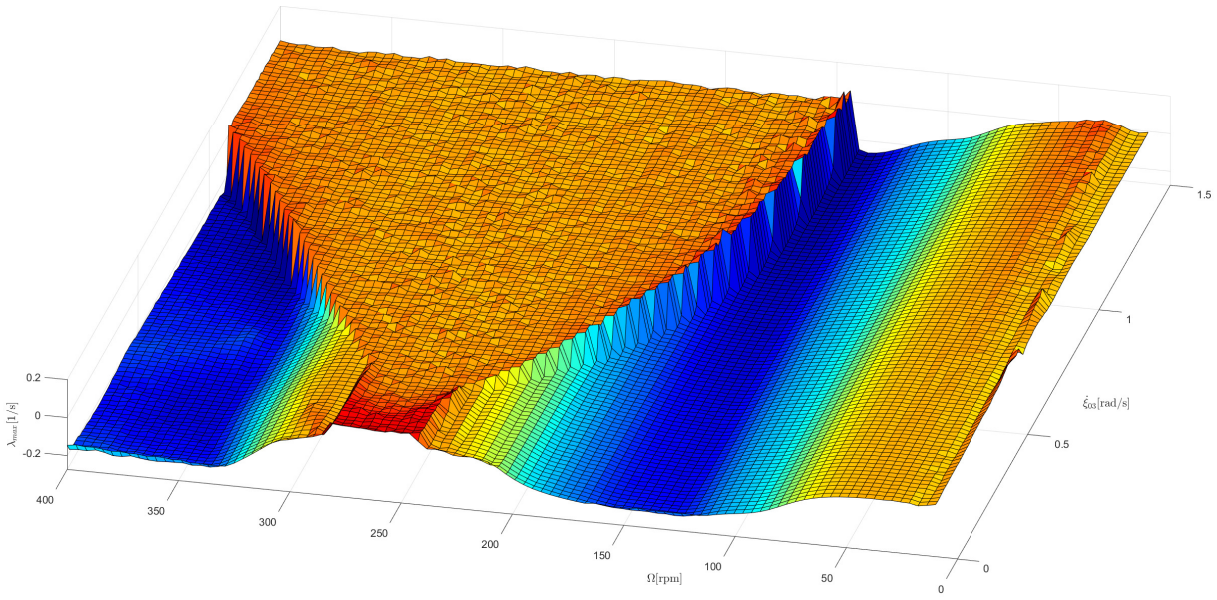

Figure 3.13: 3D plot of the MLCE with the third damper inoperative and different initial condition of $\dot{\xi}_{03}$.

3.2.3. MLCE at Fixed rpm with One Lead-Lag Damper Inoperative

The results presented in [27] in terms of LCEs are here reproduced and presented in Fig. 3.14, considering the *ad-hoc* model, which includes the geometric nonlinearities asso-

ciated with the finite motion of the parts, and the multibody model, which on top of that adds the formulation of the blade motion with respect to the absolute reference frame, in form of a set of differential-algebraic equations (DAEs). The two analyses show essentially identical results since the resulting time histories are quite similar. The stability of the trivial solution, namely zero blade lead-lag rotation and zero airframe displacement, is evaluated. The largest LCE is zero for values of the linear contribution to the characteristic moment of the damper, $-C_L\dot{\zeta}$, that range from zero to about 35% of the nominal value, indicating the existence of a limit cycle oscillation that is confirmed also in case of complete geometric nonlinearity in the kinematics of the blades. From that point on, the LCE becomes progressively negative with a steady slope, reaching a value of about -1 s^{-1} when the linear contribution $-C_L\dot{\zeta}$ reaches its nominal value. The parametric stability of the isotropic problem at fixed rpm is then studied by varying the linear contribution in Eq. (3.3), namely the term $-C_L\dot{\zeta}_i$, with $C_L \in [0, c_i]$, as proposed in [27], after the insurgence of a limit cycle for $C_L = 0$ was observed in [22].

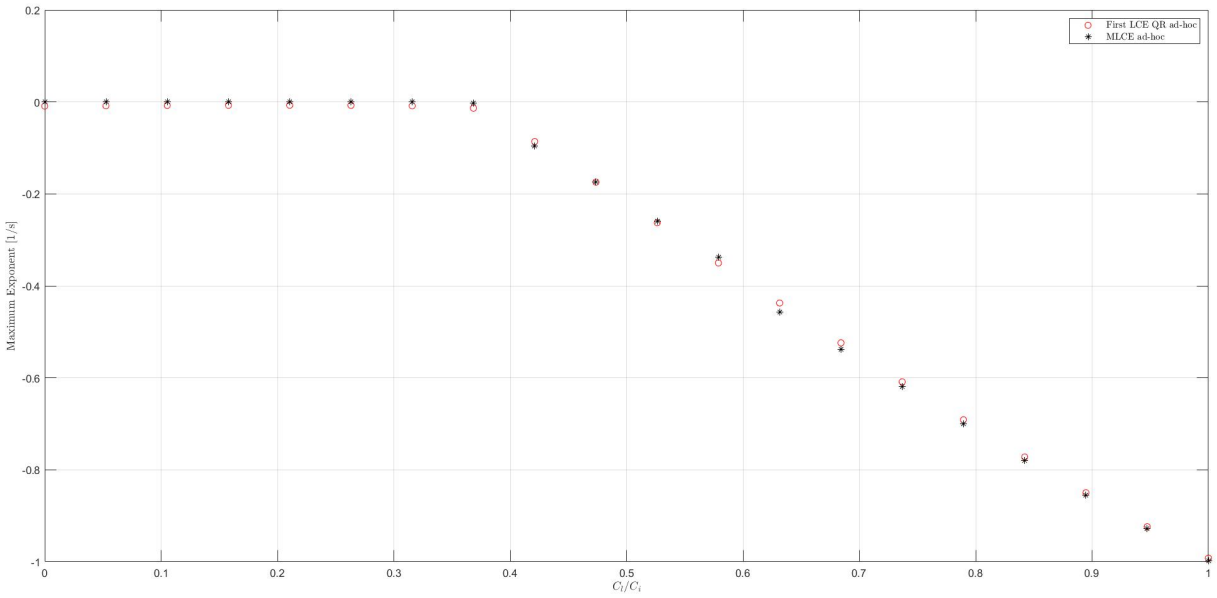

Figure 3.14: MLCE of isotropic case with nonlinear *ad-hoc* model and nonlinear damper, using discrete QR and Jacobian-less method.

3.3. Different Lead-Lag Dampers

Since one way of eliminating the classical mechanical instability is to increase the blade damping, Hammond [13] proposed to try this approach on the instability indicated in Fig. 2.4. The approach was to leave the damping identically zero on one blade and increase the damping on the remaining three blades. The results of this series of calculations are

shown in Fig. 3.15, where the region of instability is presented as a function of blade lag damping and rotor speed. As can be seen from Fig. 3.18, increasing the blade damping on all three blades with operative damper has very little effect on the stability boundaries when the remaining blade has zero damping. This result, also presented by Hammond, was somewhat expected since from the previous calculations it was observed that the blade with zero damping responds more or less independently of the other blades in the rotor. Another attempt was to increase only the characteristic of the damper acting on the opposite blade with respect to that with inoperative damper. As can be seen from Fig. 3.15, increasing that blade damping has very little effect, again as expected. The last attempt was to increase the damping on the two blades immediately adjacent to that with inoperative damper. As can be seen from Fig. 3.16, in this scenario the region of instability decreases, and disappears after a certain value of damping is reached. For the Non-isotropic Lead-Lag Damper configuration the equations of motion of the *ad-hoc* in the x hub direction (1.12a) and y hub direction (1.12b) remain unchanged. The main difference is thus in the blades equation as follows

$$\begin{aligned} &I_b\ddot{\zeta}_i - f_i(\dot{\zeta}_i) + k_i\zeta_i + e\Omega^2 S_b \sin\zeta_i \\ &- S_b[\ddot{x}_h \sin(\psi_i + \zeta_i) - \ddot{y}_h \cos(\psi_i + \zeta_i)] = 0 \quad i = 1 \dots N_b \end{aligned} \tag{3.4}$$

for each blade, where $f_i(\dot{\zeta}_i)$ is the blade damping moment, with $f_i(\dot{\zeta}_i) = -\beta_i c_i(\dot{\zeta}_i)$ but the values of $\beta_i c_i$ differ blade to blade. With $\beta_i = 1$ the nominal value is obtained.

3.3.1. Increment of the First Lead-Lag Damper Characteristic

As expected, the increment of only one damper does not change the region of instability Fig. 3.15. This is due to the fact that when the damper is inoperative the motion of the blade associated with it is very little influenced by the difference in the damping value of just one blade.

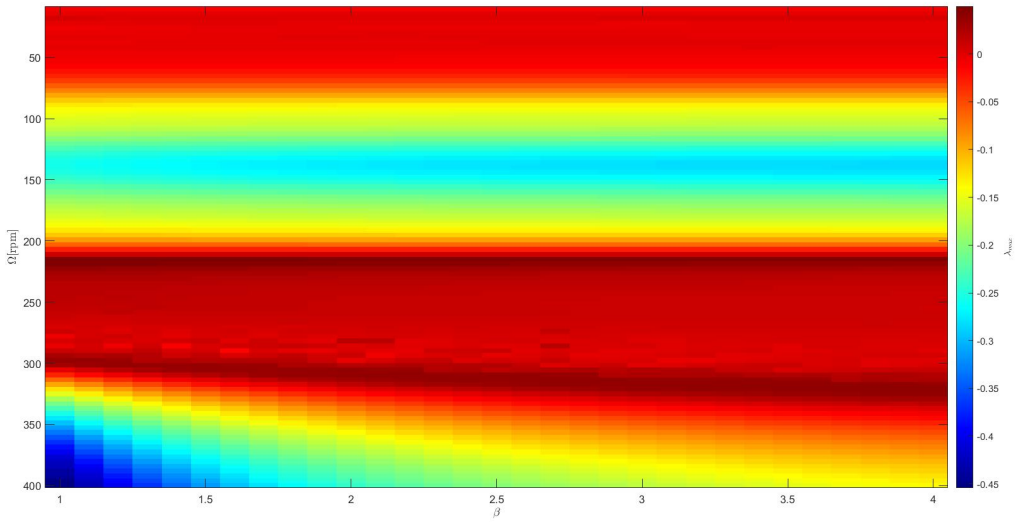

Figure 3.15: Increased characteristic of First blade Lead-Lag Damper.

3.3.2. Increment of the Second and Fourth Lead-Lag Dampers Characteristic

The increment of the dampers immediately adjacent to the inoperative one shows that the region of instability is reduced, Fig. 3.16. From $\beta \in [1, 2.5]$, the region of instability decreases; then, after $\beta = 2.5$, the systems becomes stable. This can also be observed in Fig. 3.17.

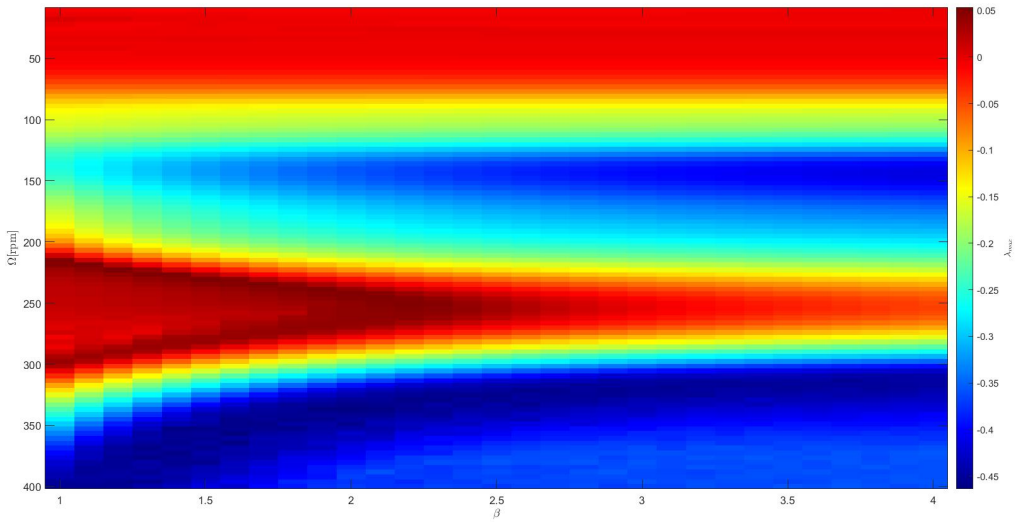

Figure 3.16: Increased characteristic of second and fourth blade Lead-Lag Dampers.

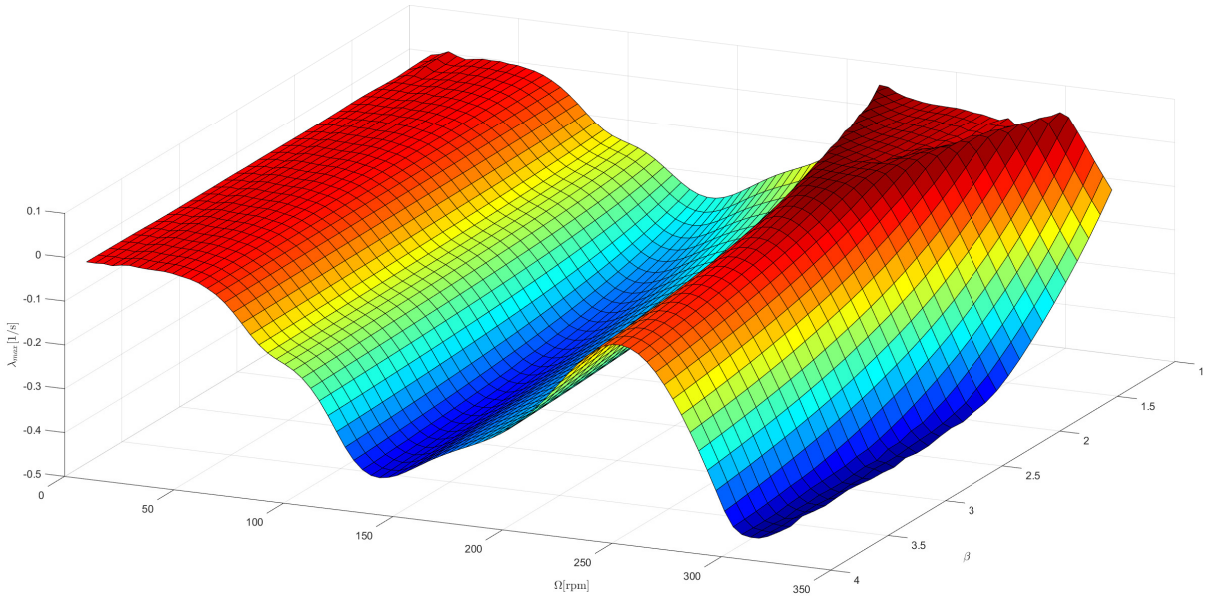

Figure 3.17: 3D plot, Increased characteristic of second and fourth blade Lead-Lag Dampers with different c_i.

3.3.3. Increment of the First, Second and Fourth Lead-Lag Dampers Characteristic

The increment of all operative dampers does not change the region of instability, as shown in Fig. 3.18. For $\beta \in [1, 2]$ there is a reduction of the region of instability, but for $\beta \geq 2$ the region does not reduce any more, so the instability remains, as already pointed out by Hammond.

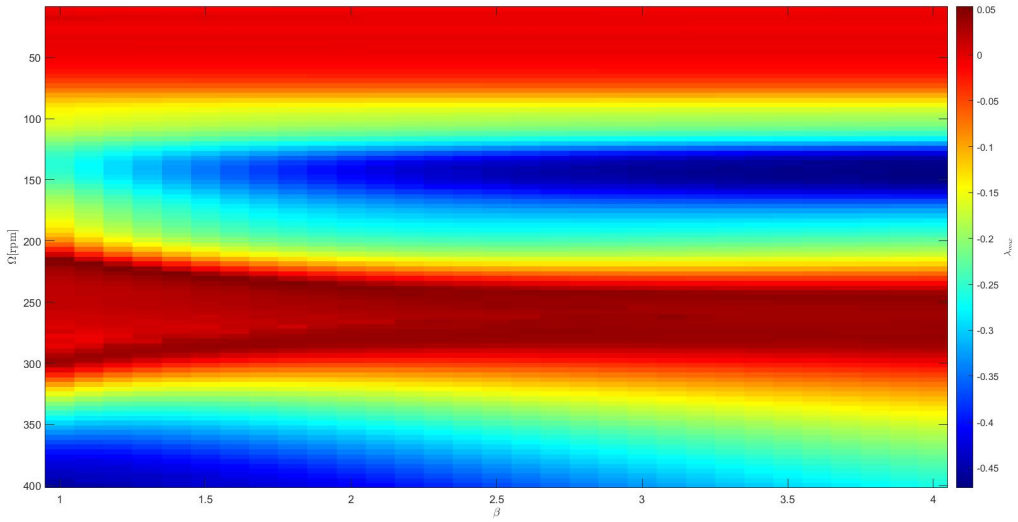

Figure 3.18: Increased characteristic of first, second and fourth blade Lead-Lag Dampers.

The result highlighted in this Section, namely the fact that using different amounts of damping may guarantee the stability of the system also in case of failure of a damper, is not of immediate practical use. However, it suggests that the loss of stability in case of damper failure is somewhat associated with the complete loss of damping of a blade, in case of failure, whereas some form of "cooperation" of the remaining blades, with intact damping, could help mitigate the loss of stability. A possible cure is discussed in the following sections.

3.4. The Inter-Blade Lead-Lag Damper Model

A different approach for damping the lead-lag motion of rotor blades is used in some helicopters. It consists of a different damper connection configuration, that of Inter-Blade Lead-Lag dampers (3.4.1). This type of damper arrangement is present in some designs; examples of its use are the Saunders-Roe Skeeter, NHIndustries NH90, Airbus H155 (Fig. 3.19), Leonardo AW169, and Kopter AW09 (Fig. 3.20).

Figure 3.19: Rotor of the Airbus H155, Inter-Blade.

Figure 3.20: Rotor of the Kopter AW09, Inter-Blade configuration with an elastomeric damper.

Among the advantages of the Inter-Blade damper is that it does not introduce damping

associated with the collective lag motion. This means that elastomeric dampers can be used without the drawback of having to withstand the steady loads associated with steady collective lag. At the same time, the inter-blade damper magnifies the amount of damping applied to each blade resulting from the cyclic modes: three times for a 3-blade rotor, two times for a 4-blade rotor, and so on. A drawback is that an enormous amount of damping, four times the damper's nominal value, is associated with the reactionless mode, which requires none. Another way of introducing lead-lag damping has been recently presented [12], the Inter-2-Blade damper configuration (discussed in Section 3.4.2). It works between opposite blades.

In case of failure of a single damper, this type of design should reduce the region of instability, since the rotor just loses one part of the damping, but all blades are somewhat subjected to some amount of damping. Usually, this type of dampers is made of elastomeric material; however, for the present analysis, the dampers are considered linear viscous for simplicity. Further research can be developed, considering nonlinear constitutive laws for modeling nonlinear dampers (see Section 3.2).

3.4.1. Inter-Blade Lead-Lag Damper

For the inter-blade Lead-Lag Damper configuration, the equations of motion of the *ad-hoc* model in the x hub direction (1.12a) and y hub direction (1.12b) remain unchanged. The main difference is thus in the blades equation as follows

$$\begin{aligned} &I_b\ddot{\zeta}_i - f_i(\dot{\zeta}_i, \dot{\zeta}_{i+1}, \dot{\zeta}_{i-1}) + k_i\zeta_i + e\Omega^2 S_b \sin\zeta_i \\ &- S_b[\ddot{x}_h \sin(\psi_i + \zeta_i) - \ddot{y}_h \cos(\psi_i + \zeta_i)] = 0 \quad i = 1 \dots N_b \end{aligned} \tag{3.5}$$

for each blade, where $f_i(\dot{\zeta}_i, \dot{\zeta}_{i+1}, \dot{\zeta}_{i-1})$ is the blade damping moment, with $f_i(\dot{\zeta}_i, \dot{\zeta}_{i+1}, \dot{\zeta}_{i-1}) = -\frac{c_i}{2}(\dot{\zeta}_i - \dot{\zeta}_{i-1}) - \frac{c_i}{2}(\dot{\zeta}_i - \dot{\zeta}_{i+1})$ when the linear damper of [13] is considered. The numerical data proposed in [13] is considered also in this case. By using Deutsch's criterion [9], as generalized in [12] for the inter-blade configuration, for the value of the damper, an estimation of $c_{ib} = \frac{c_i}{2}$ where c_i is the nominal value of the Hammond model, Table 1.1.

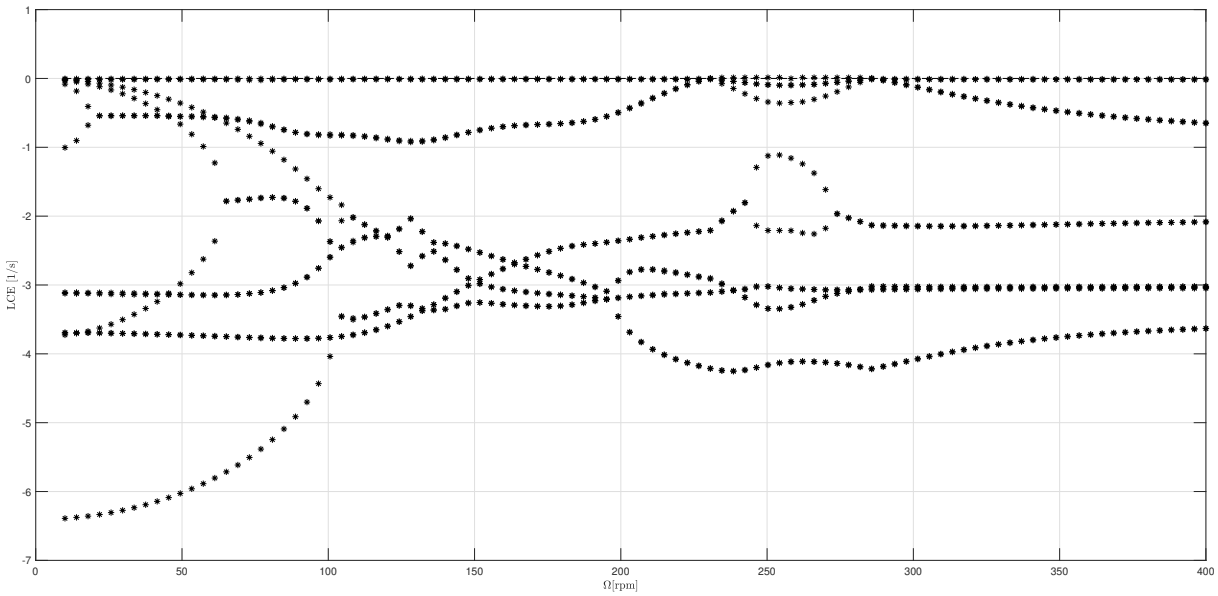

Figure 3.21: LCEs of Inter-Blade Damper configuration with one damper inoperative.

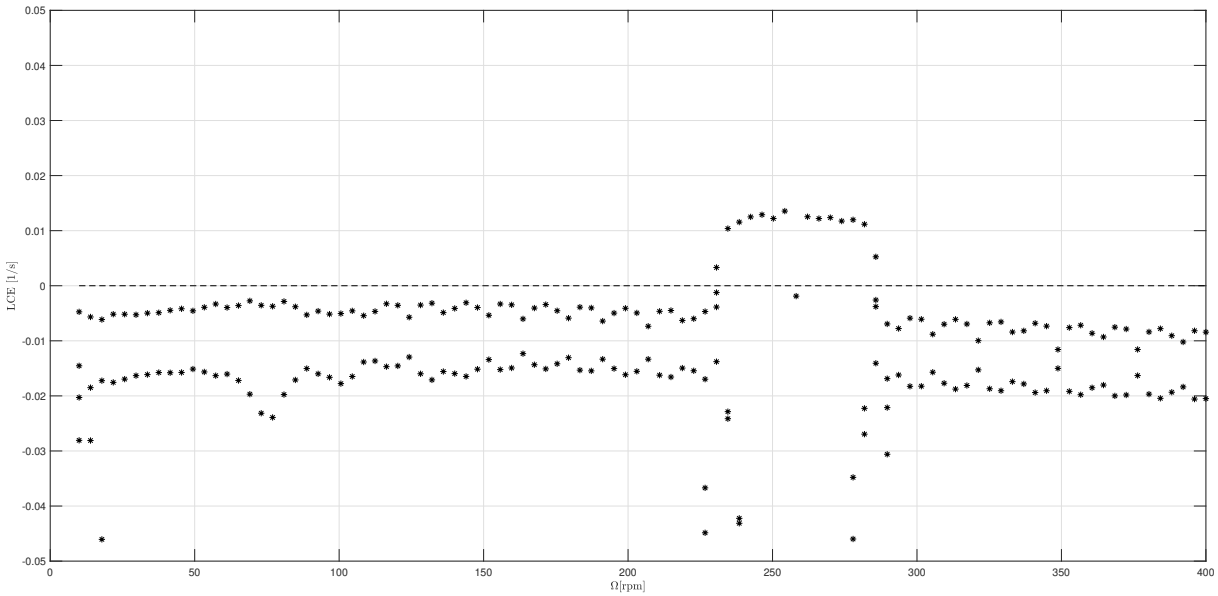

Figure 3.22: LCEs of Inter-Blade Damper configuration with one damper inoperative, zoom of the unstable LCEs.

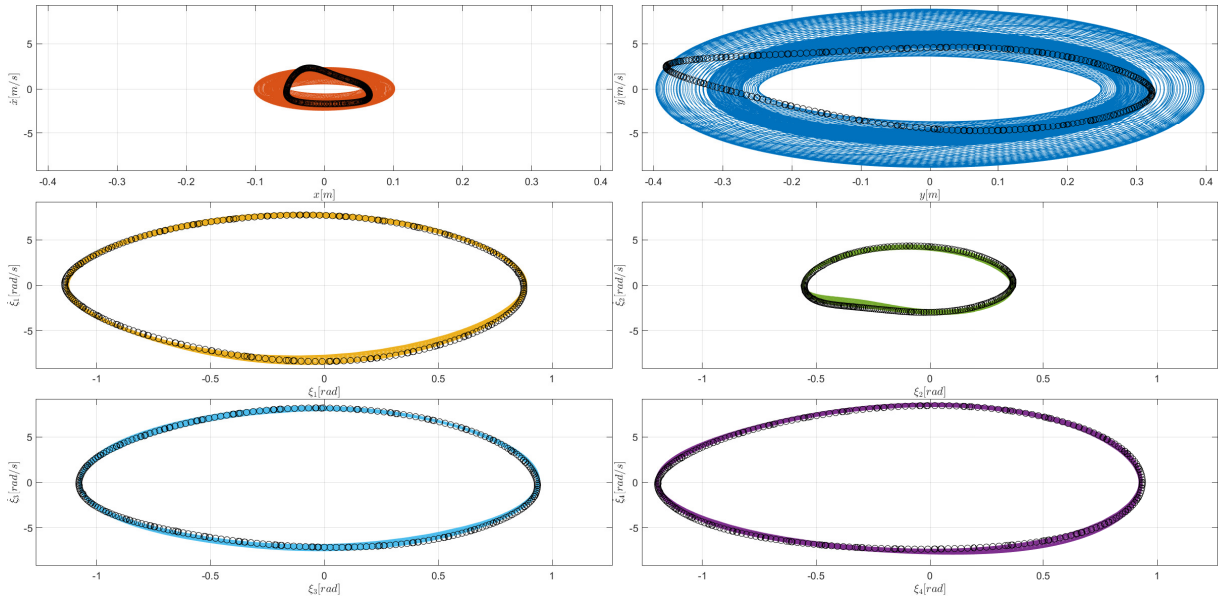

Figure 3.23: Phase space of Inter-Blade Damper configuration at $\Omega = 250$ rpm.

3.4.2. Inter-2-Blade Lead-Lag Damper

For the Inter-2-Blade Lead-Lag Damper configuration, the equations of motion of the *ad-hoc* model in the x hub direction (1.12a) and y hub direction (1.12b) remain unchanged. The main difference is thus in the blades equation as follows

$$\begin{aligned} &I_b\ddot{\zeta}_i - f_i(\dot{\zeta}_i, \dot{\zeta}_{i-2}, \dot{\zeta}_{i+2}) + k_i\zeta_i + e\Omega^2 S_b \sin\zeta_i \\ &- S_b[\ddot{x}_h \sin(\psi_i + \zeta_i) - \ddot{y}_h \cos(\psi_i + \zeta_i)] = 0 \quad i = 1 \dots N_b \end{aligned} \tag{3.6}$$

for each blade, where $f_i(\dot{\zeta}_i, \dot{\zeta}_{i-2}, \dot{\zeta}_{i+2})$ is the blade damping moment, with $f_i(\dot{\zeta}_i, \dot{\zeta}_{i-2}, \dot{\zeta}_{i+2}) = -\frac{c_i}{4}(\dot{\zeta}_i - \dot{\zeta}_{i-2}) - \frac{c_i}{4}(\dot{\zeta}_i - \dot{\zeta}_{i+2})$ when the linear damper of [13] is considered. The numerical data proposed in [13] is considered also in this case. By using Deutsch's criterion, generalized to the inter-2-blade configuration as proposed [12], the value of $c_{i2b} = \frac{c_i}{4}$ for the damper characteristic is obtained, where c_i is the nominal value of the Hammond model, Table 1.1. This type of configuration has not been implemented in a helicopter, yet, but it should be more fail-safe. The LCEs method, when one damper is inoperative, gives a smaller region of instability as to the Inter-Blade configuration, Fig. 3.25.

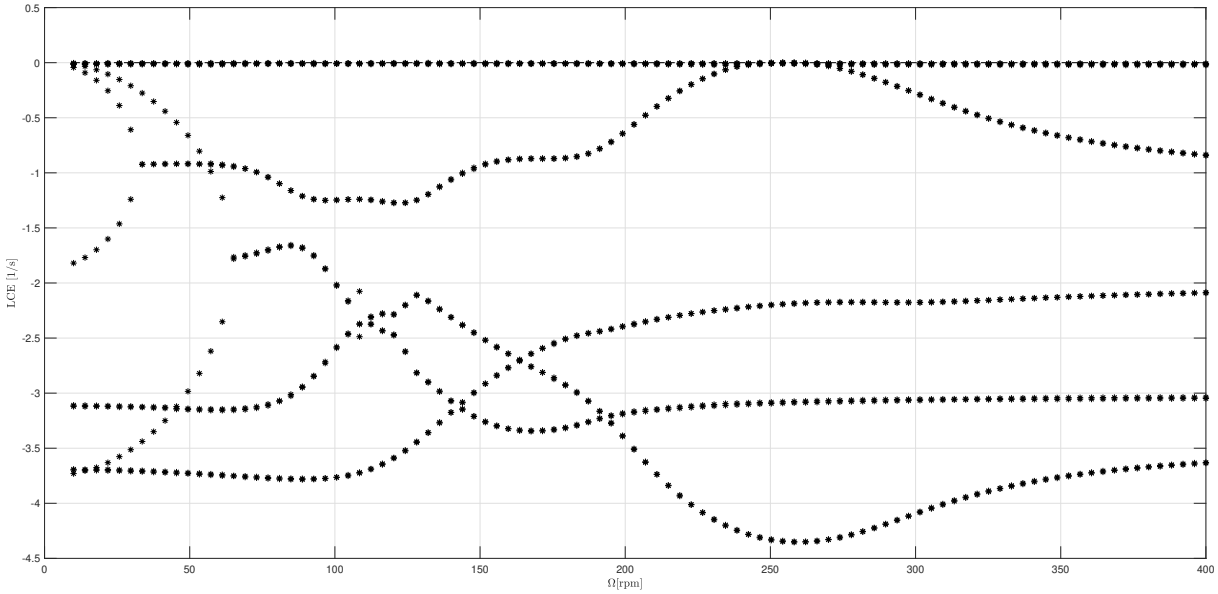

Figure 3.24: LCEs of Inter-2-Blade Damper configuration with one damper inoperative.

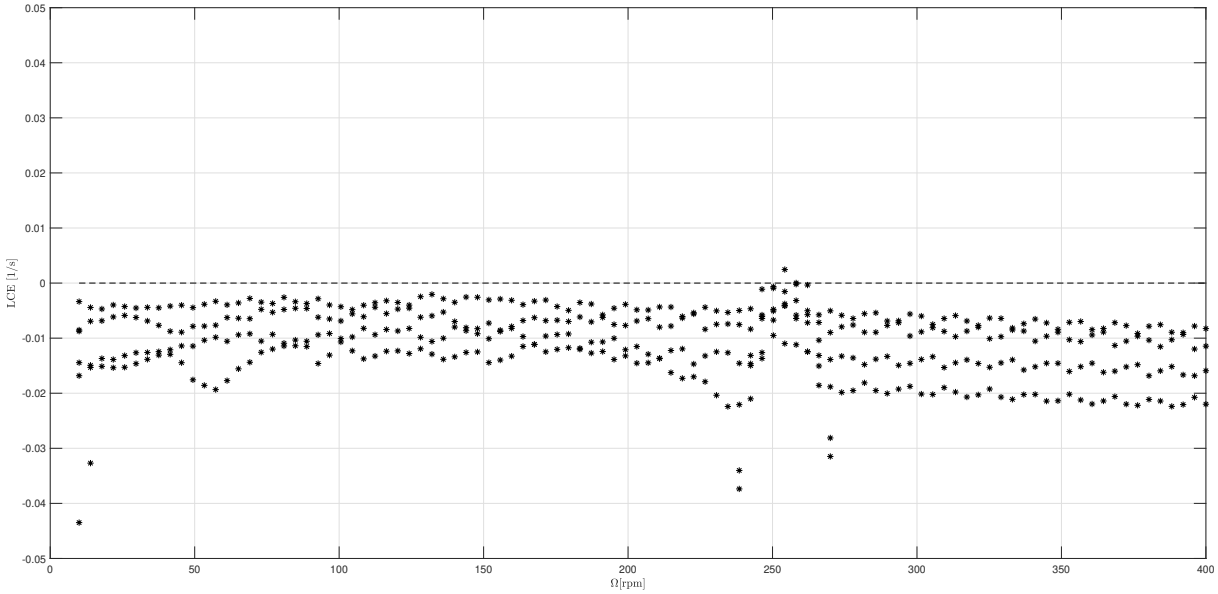

Figure 3.25: LCEs of Inter-2-Blade Damper configuration with one damper inoperative, zoom of the unstable LCEs.

If the value of the damper characteristic is increased, it can be shown that the region of instability decreases with the increase of the operative dampers' characteristic (Fig. 3.26). This should be expected since when one damper is inoperative, the relative blades still have half of the nominal damping, as opposed to the conventional arrangement used in Hammond's model, where if one damper is inoperative the related blade has no damping. the Inter-2-Blade configuration for this reason should be more fail-safe.

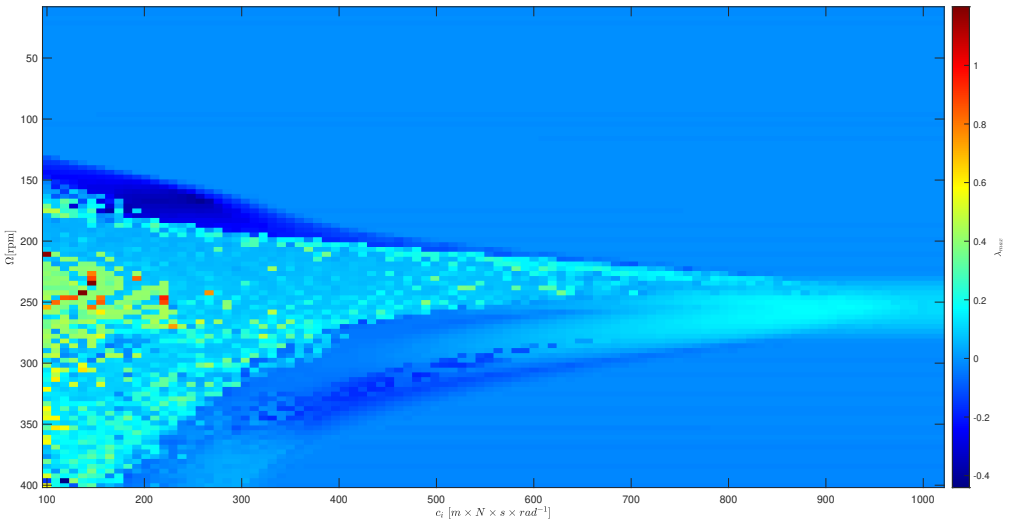

Figure 3.26: MLCEs of Inter-2-Blade Damper configuration with different value of c_i.

3.5. Tiltrotor Model, Whirl-Flutter Stability

So far, the analysis focused on a full-featured, yet relatively simple rotorcraft model, restricted to rigid blades with only the lead-lag degree of freedom in addition to two components of airframe motion. To explore the ability to estimate the MLCE also from a more complex system, the problem of tiltrotor whirl flutter analysis has been addressed, exploiting the availability of a rather sophisticated multibody model implemented in MB-Dyn [4]. This model, shown in Fig. 3.27, was developed by Alessandro Cocco within the CleanSky2 project ATTILA. It is used for the design of a wind-tunnel model of the Next Generation Civil Tiltrotor (NGCTR) concept. In [4], its aeroelastic stability was studied using the Periodic Operational Modal Analysis (POMA). Such results are used as reference for comparison with those obtained using the MLCE method.

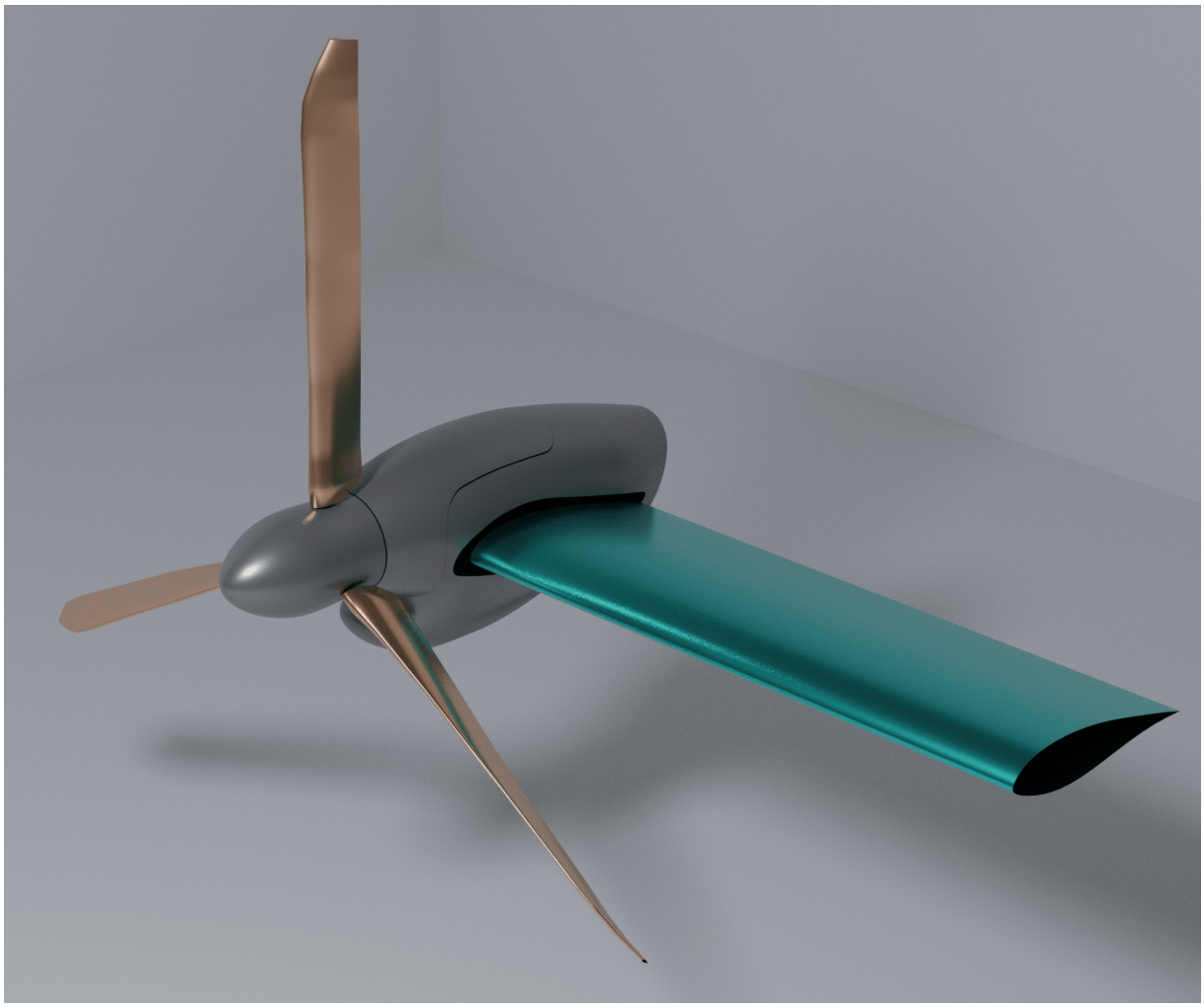

Figure 3.27: ATTILA model.

Tiltrotor design remains a rather challenging engineering task, considering the various operating conditions and multipurpose missions that are expected to be accomplished by this complex type of aircraft. In particular, the problem of assessing whirl-flutter stability limits is at the same time fundamental and challenging. Whirl-flutter is an aeroelastic stability phenomenon that affects both turboprop and tiltrotor aircraft. When a rotor mounted on a flexible structure rotates, the normal vibration modes associated with the supporting structure may interact with the precession motion of the rotor. When its motion is perturbed, each point on the rotor axis of rotation draws paths about its reference position. This motion changes the way each rotor blade is affected by the incoming airspeed, correspondingly altering the overall aerodynamic loads. At the verge of whirl flutter, when this phenomenon is triggered, perturbations may result in a periodic orbit. The resulting oscillatory loads can lead to the divergence of the system response, in what represents a truly aeroelastic instability.

The wing model consists of 3 finite-volume three-node beam elements for the stiffness part, and one body element for each node to model the inertial component. The nacelle part is divided into a tilting and a non-tilting part, both modeled as rigid bodies The parts are connected with deformable joints, which represent the flexibility of downstop and wing-pylon attachments. The aerodynamic loads are introduced through MBDyn's aerodynamic beam elements, based on simple strip theory, each linked to the corresponding structural element. The ATTILA proprotor is a three-bladed stiff-in-plane rotor (Fig. 3.28) with a gimballed hub. It consists of the control chain, three blades, and the yoke.

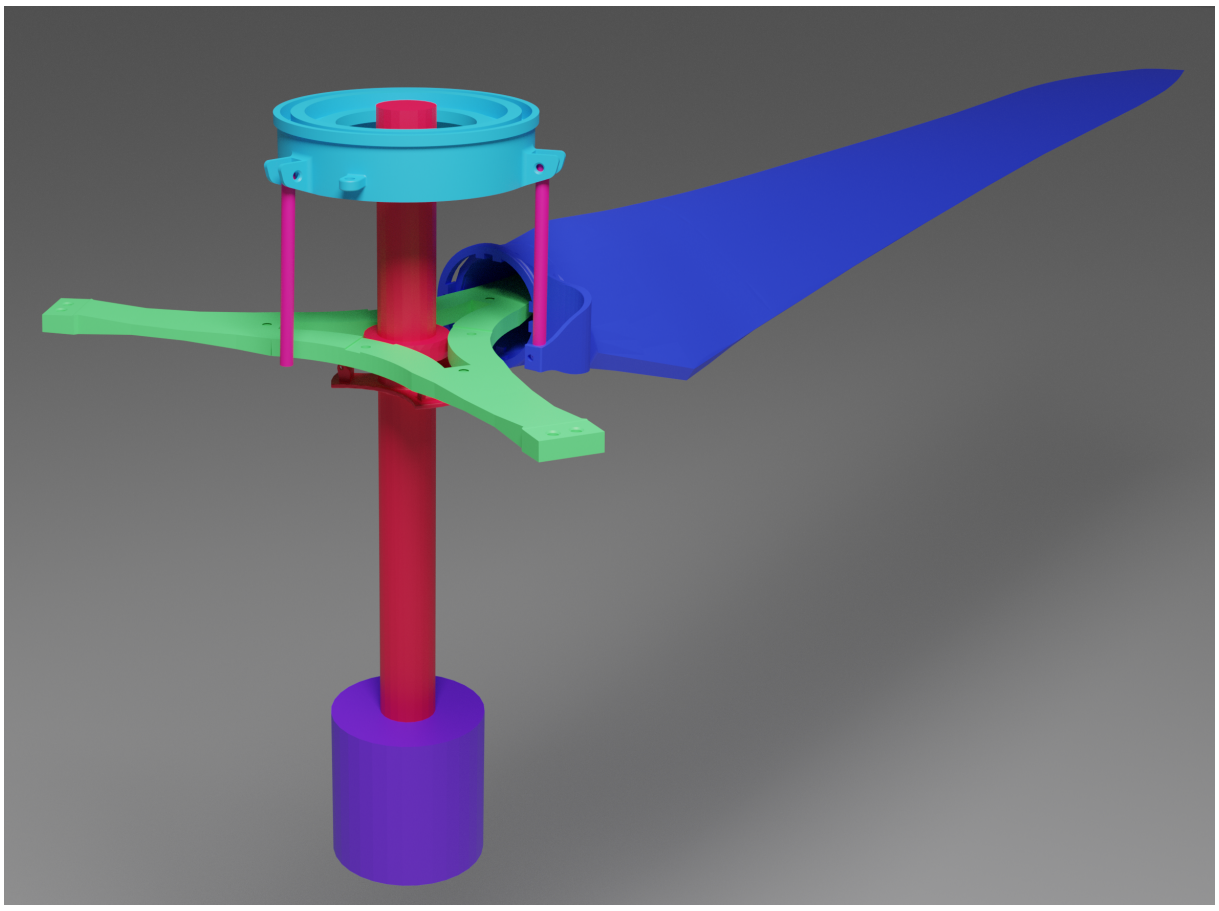

Figure 3.28: MBDyn rotor model: engine (purple), yoke (green), mast (red), swash-plate (cyan), blade (blue), pitch link (magenta).

An external force is introduced to excite the system. The results obtained from the time series in the x direction (Fig. 3.29) and y direction (Fig. 3.30) show a trend that follows the results in the chord direction obtained with POMA analysis [4], with a difference due to the fact that the MLCE method analyzes the time series, so all the contributions are present. The results obtained from the time series in the z direction (Fig. 3.31) follow

the results in the bending direction obtained with POMA analysis [4]. They also have a contribution from the torsion, so the results are not identical, but they are very similar. Further studies need to be conducted on the type of exciting force needed to obtain other modes.

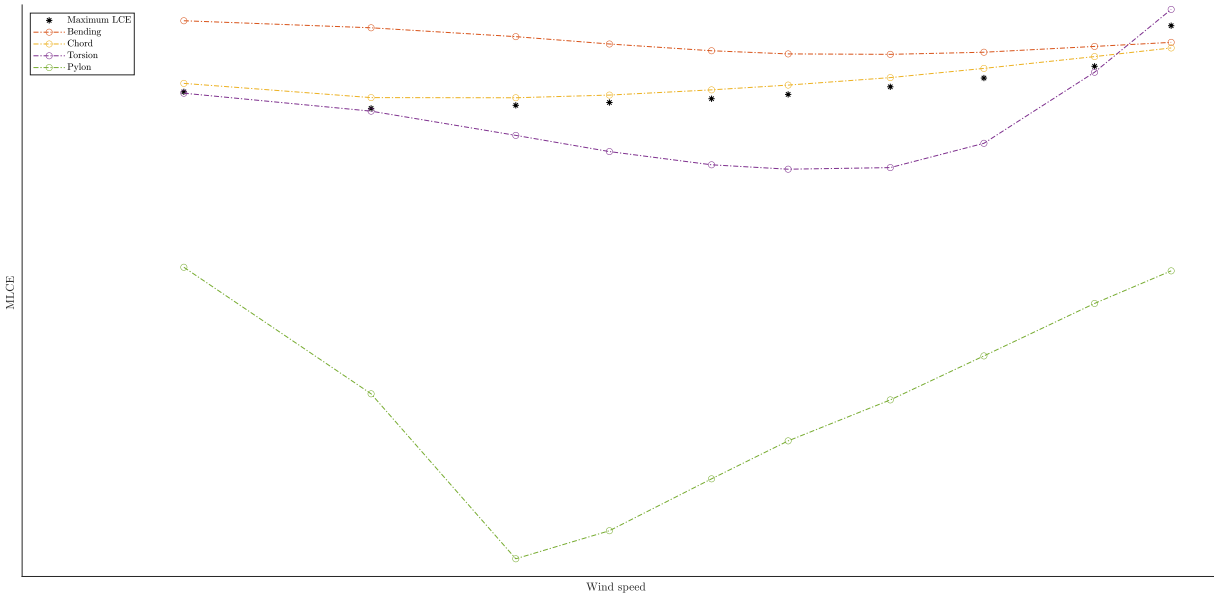

Figure 3.29: MLCE of the Tiltrotor for the time series of the displacement in the x direction with different values of the wind speed and external excitation force, compared with the POMA analysis.

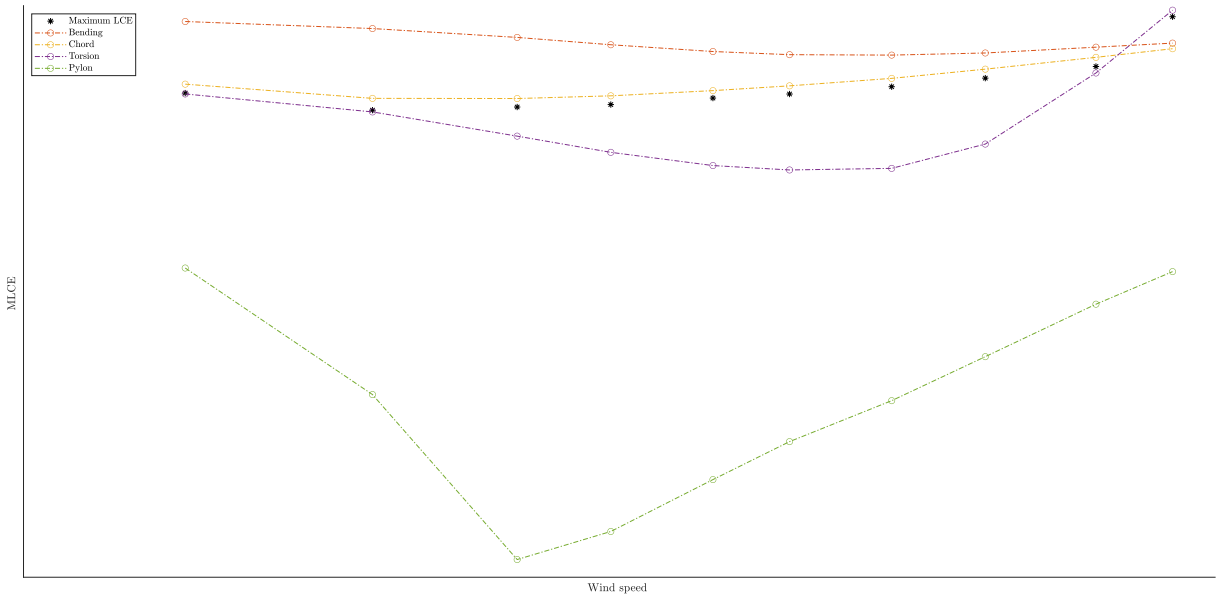

Figure 3.30: MLCE of the Tiltrotor for the time series of the displacement in the y direction with different values of the wind speed and external excitation force, compared with the POMA analysis.

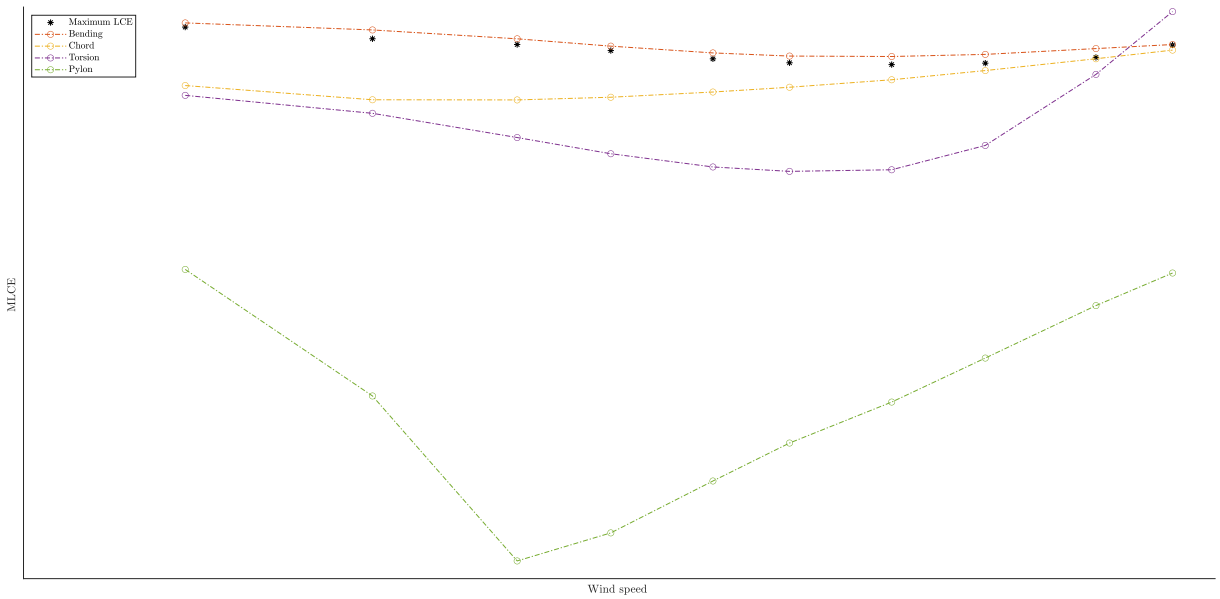

Figure 3.31: MLCE of the Tiltrotor for the time series of the displacement in the z direction with different values of the wind speed and external excitation force, compared with the POMA analysis.

Another way to use the MLCE is by first applying the POD (Proper orthogonal decomposition) to a combination of signals, to extract the most energetic signals from the time

response of the system, then applying the MLCE method to each principal signal. In this way, the different contributions are separated. The results are sorted in order of decreasing singular values.

The first is dominated by chordwise bending response (Fig. 3.32), the second one by flatwise bending response (Fig. 3.33) and, lastly, the third by torsional response (Fig. 3.34). One disadvantage of using the MLCE in this type of analysis is that the result is strongly dependent on the sampling window and can vary depending on the changes in the parameters. Nevertheless, the results give an approximate analysis coherent with the one obtained with the POMA analysis.

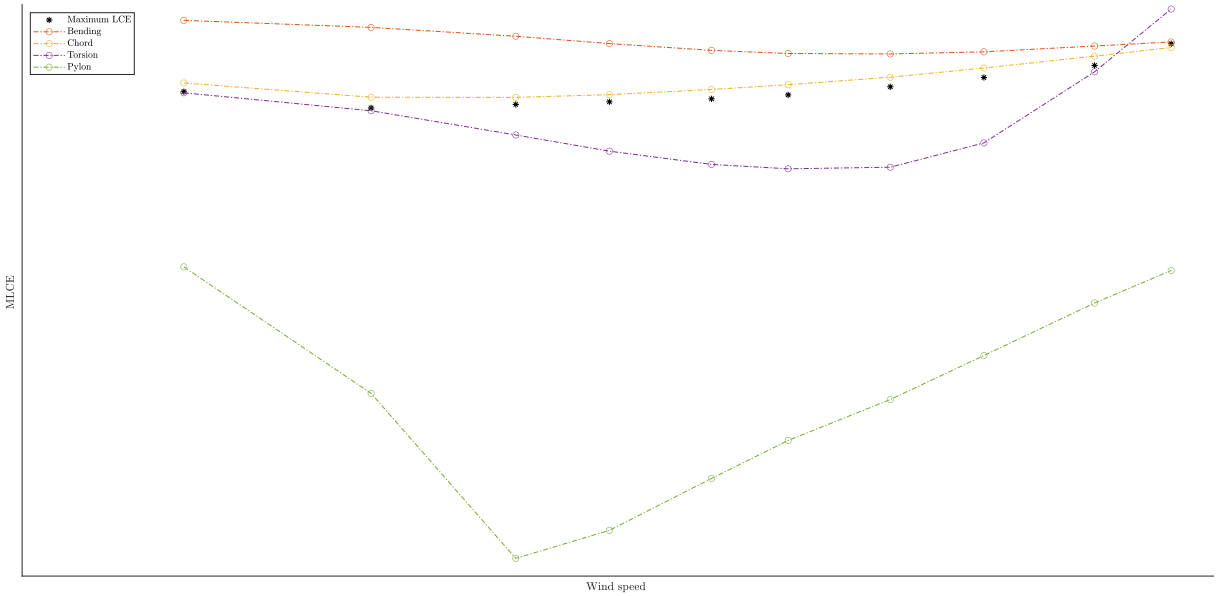

Figure 3.32: MLCE obtained by the time history of the first singular value from the POD, compared with the POMA analysis.

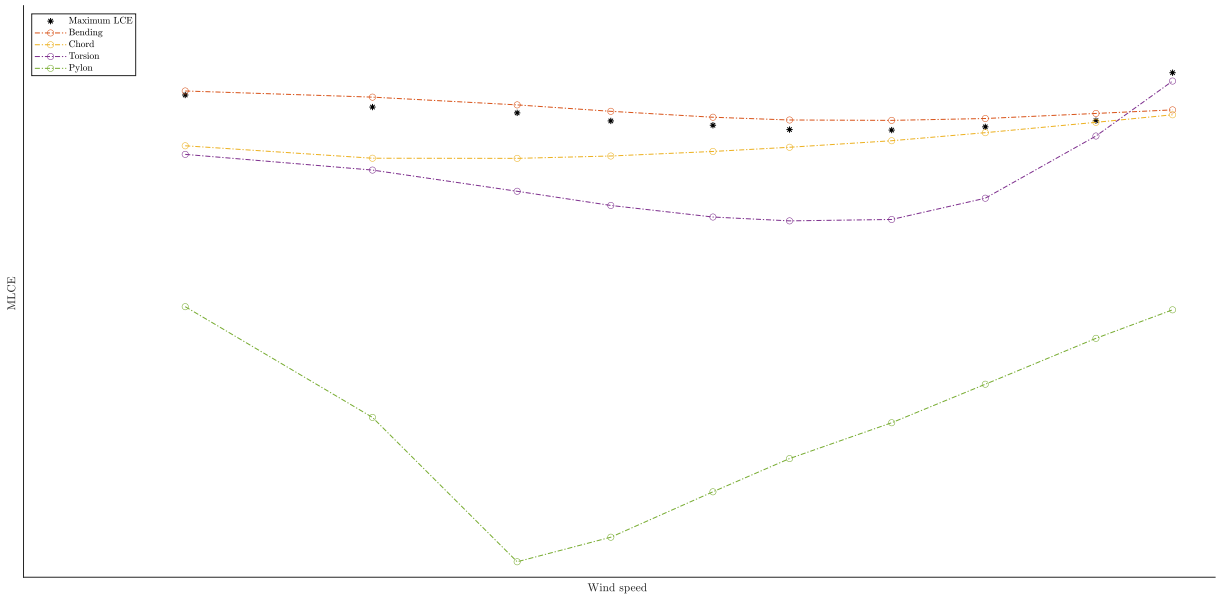

Figure 3.33: MLCE obtained by the time history of the second singular value from the POD, compared with the POMA analysis.

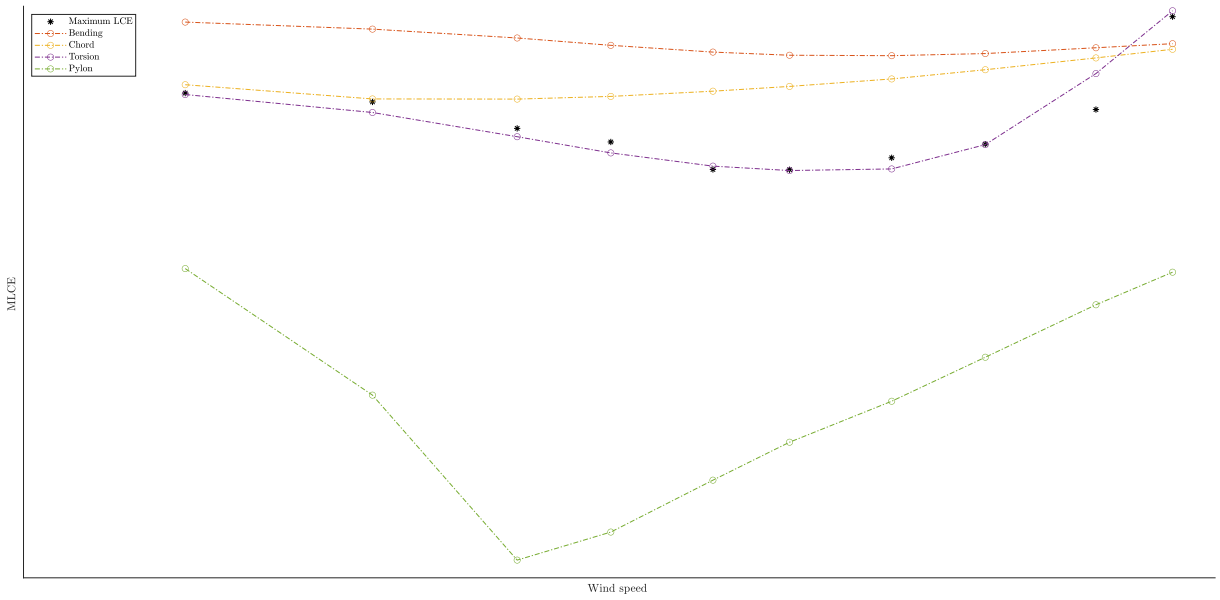

Figure 3.34: MLCE obtained by the time history of the third singular value from the POD, compared with the POMA analysis.

4 | Conclusion

This thesis shows the use of LCEs to study the Ground Resonance phenomenon. The results of Fig. 2.4 show that the method gives an accurate indication of the type of dynamical instability that occurs in Ground Resonance. The LCEs method was also implemented for more complex cases as for the Inter-Blade Lead-Lag configuration (Section 3.4.1) and the Inter-2-Blade Lead-Lag configuration (Section 3.4.2). The method's strength is that can provide a stability analysis even for systems that do not have periodicity or are strongly non-linear, whereas Floquet's method (Section 2.1) fails. A drawback is the computational cost of performing this type of analysis. This is because, to have an accurate estimate, the time series need to be long and the problem also scales with the degrees of freedom very quickly. One way to ensure the convergence of the LCEs is by putting a residual between time steps and stopping until a threshold is reached. A way to make a stability analysis more computationally advantageous is by only computing the MLCE (Section 2.4.2). With this method, also the knowledge of the Jacobian matrix is no longer necessary. For this reason, it was implemented in MBDyn (Section 3.1) to show the potential of the method. One drawback of the method is the necessity of estimating some parameters a priori, i.e., the embedding dimension and the time delay. Then the method was applied to a more complex system, to show the potential application in MBDyn (Sections 3.5 and 3.2). The main objective of this thesis was to show the possible application of LCEs and MLCE in multibody dynamics with a focus on the Ground Resonance problem.

Bibliography

[1] G. Benettin, L. Galgani, A. Giorgilli, and J. Strelcyn. Lyapunov characteristic exponents for smooth dynamical systems and for hamiltonian systems; a method for computing all of them. part 2: Numerical application. *Meccanica*, 15: 197–231, 1980/03/01. doi: 10.1007/BF02128237. URL https://doi.org/10.1007/BF02128237.

[2] W. G. Bousman, D. L. Sharpe, and R. A. Ormiston. An experimental study of techniques for increasing the lead-lag damping of soft inplane hingeless rotors. 1976.

[3] S. Cardinale, R. Donham, and I. Sachs. *Ground and air resonance characteristics of a soft in-plane rigid-rotor system*. doi: 10.2514/6.1969-205. URL https://arc.aiaa.org/doi/abs/10.2514/6.1969-205.

[4] A. Cocco, S. Mazzetti, P. Masarati, S. van't Hoff, and B. Timmerman. Numerical whirl-flutter analysis of a tiltrotorsemi-span wind tunnel model. 2022.

[5] R. Coleman. Theory of self-excited mechanical oscillations of hinged rotor blades. ARR 3G29, NACA, July 1943.

[6] R. Coleman and A. Feingold. Theory of self-excited mechanical oscillations of helicopter rotors with hinged blades. *NACA Report 1351*, 1958.

[7] J. A. I. da Silva, D. D. Bueno, and G. L. de Abreu. A strategy to suppress limit cycle oscillations in helicopter ground resonance including landing gear nonlinearities. *Aerospace Science and Technology*, 105:106011, 2020. ISSN 1270-9638. doi: https://doi.org/10.1016/j.ast.2020.106011. URL https://www.sciencedirect.com/science/article/pii/S1270963820306933.

[8] S. G. Dawson. An experimental investigation of the stability of a bearingless model rotor in hover. *Journal of The American Helicopter Society*, 28:29–34, 1983.

[9] M. L. Deutsch. Ground vibrations of helicopters. *Journal of the Aeronautical Sciences*, 13(5):223–228, 1946. doi: 10.2514/8.11359. URL https://doi.org/10.2514/8.11359.

[10] L. Dieci. Jacobian free computation of lyapunov exponents. *Journal of Dynamics and Differential Equations*, 14:697–717, 2002.

[11] G. Floquet. Sur les équations différentielles linéaires à coefficients périodiques. *Annales scientifiques de l'École Normale Supérieure*, 2e série, 12:47–88, 1883. doi: 10.24033/asens.220. URL `http://www.numdam.org/articles/10.24033/asens.220/`.

[12] L. Frison, A. Zanoni, and P. Masarati. The inter-2-blade lead-lag damper concept. Fort Worth, TX, USA, May 20-22 2022.

[13] C. Hammond. An application of Floquet theory to prediction of mechanical instability. *Journal of the American Helicopter Society*, 19(4):14–23, 1974. doi:10.4050/JAHS.19.14.

[14] D. H. Hodges. An aeromechanical stability analysis for bearingless rotor helicopters. *Journal of The American Helicopter Society*, 24:2–9, 1978.

[15] J. Kelliher. Oseledec's multiplicative ergodic theorem. *UT Austin*.

[16] D. Kunz. Nonlinear analysis of helicopter ground resonance. *Nonlinear Analysis: Real World Applications*, 3:383–395, 09 2002. doi: 10.1016/S1468-1218(01)00037-2.

[17] G. Leonov and N. Kuznetsov. Time-varying linearization and the perron effects. *International Journal of Bifurcation and Chaos*, 17:1079–1107, 11 2007. doi: 10.1142/S0218127407017732.

[18] R. T. Lytwyn, W. Miao, and W. Woitsch. Airborne and ground resonance of hingeless rotors. *Journal of the American Helicopter Society*, 16(2):2–9, 1971. ISSN 2161-6027. doi: doi:10.4050/JAHS.16.2.2. URL `https://www.ingentaconnect.com/content/ahs/jahs/1971/00000016/00000002/art00001`.

[19] P. Masarati. Estimation of lyapunov exponents from multibody dynamics in differential-algebraic form. *Proceedings of the Institution of Mechanical Engineers, Part K: Journal of Multi-body Dynamics*, 227:23–33, 03 2013. doi: 10.1177/1464419312455754.

[20] J. Mawhin. *Alexandr Mikhailovich Liapunov, The general problem of the stability of motion (1892)*, pages 664–676. 01 2005.

[21] M. Pollicott. *References*, page 155–160. London Mathematical Society Lecture Note Series. Cambridge University Press, 1993. doi: 10.1017/CBO9780511752537.012.

[22] G. Quaranta, V. Muscarello, and P. Masarati. Lead-lag damper robustness analysis

for helicopter ground resonance. *Journal of Guidance Control and Dynamics*, 36: 1150–1161, 2013.

[23] M. T. Rosenstein, J. J. Collins, and C. J. De Luca. A practical method for calculating largest lyapunov exponents from small data sets. *Physica D: Nonlinear Phenomena*, 65(1):117–134, 1993. ISSN 0167-2789. doi: https://doi.org/10.1016/0167-2789(93)90009-P. URL https://www.sciencedirect.com/science/article/pii/016727899390009P.

[24] G. E. Santoro. Introduction to floquet. *SISSA*.

[25] C. Skokos. The lyapunov characteristic exponents and their computation. *Lecture Notes in Physics*, page 63, 11 2008. doi: 10.1007/978-3-642-04458-8_2.

[26] W. Squire and G. Trapp. Using complex variables to estimate derivatives of real functions. *SIAM Review*, 40(1):110–112, 1998. doi: 10.1137/S003614459631241X. URL https://doi.org/10.1137/S003614459631241X.

[27] A. Tamer and P. Masarati. Stability of nonlinear, time-dependent rotorcraft systems using lyapunov characteristic exponents. *Journal of the American Helicopter Society*, 61, 04 2016. doi: 10.4050/JAHS.61.022003.

[28] O. VI. A multiplicative ergodic theorem: Lyapunov characteristic numbers for dynamical systems. *Trans Moscow Math Soc*, 19:197–231, 1968.

A | Numerical Jacobian Method

One method to approximate the Jacobian matrix is to estimate it by numerical approximation. By using the Dieci algorithm[10] is possible to estimate all the LCEs without the knowledge of the Jacobian matrix, but this method still required the knowledge of the system. This is not always possible so other methods (2.4.2) need to be used if the system cannot be accessed. The algorithm starts from the equation 2.5

$$\dot{\vec{w}}(t) = \frac{\partial \vec{f}}{\partial \vec{x}^T}(\vec{x}(t)) \cdot \vec{w}(t) \tag{A.1}$$

$$\dot{\vec{w}}_{j+1}(t_{j+1}) = \frac{\partial \vec{f}}{\partial \vec{x}^T}(\vec{x}(tj+1)) \cdot \vec{w}_{j+1}(t_{j+1}) \tag{A.2}$$

this can be rewritten into $\mathbf{W} = [\vec{w}_1, ..., \vec{w}_p]$:

$$\dot{\mathbf{W}}_{j+1} = \frac{\partial \vec{f}}{\partial \vec{x}^T}(\vec{x}(t))\mathbf{W}_{j+1} \tag{A.3}$$

approximation with Forward Euler so the equation (A.3) becomes :

$$\mathbf{W}_{j+1}(t_{j+1}) - \mathbf{W}_{j+1}(t_j) \approx h\frac{\partial \vec{f}}{\partial \vec{x}^T}(\vec{x}_j)\mathbf{W}_{j+1}(t_j) \tag{A.4}$$

$$\mathbf{W}_{j+1}(t_{j+1}) = h\frac{\partial \vec{f}}{\partial \vec{x}^T}(\vec{x}_j)\mathbf{W}_{j+1}(t_j) + \mathbf{W}_{j+1}(t_j) \tag{A.5}$$

where $\mathbf{W}_{j+1}(t_j) = \mathbf{Q}_j$

$$\mathbf{W}_{j+1}(t_{j+1}) = h\frac{\partial \vec{f}}{\partial \vec{x}^T}(\vec{x}_j)\mathbf{Q}_j + \mathbf{Q}_j \tag{A.6}$$

We have the matrix multiplication $\frac{\partial \vec{f}}{\partial \vec{x}^T}(\vec{x}_j)\mathbf{Q}_j$, where $\mathbf{Q}_j = [\vec{q}_1^j, ..., \vec{q}_p^j]$ for $k = 1, ..., p$, we then approximate the action $h\frac{\partial \vec{f}}{\partial \vec{x}^T}(\vec{x}_j)q_k^j$ as

$$h\frac{\partial \vec{f}}{\partial \vec{x}^T}(\vec{x}_j)\vec{q}_k^j \approx f(\vec{x}_j + h\vec{q}_k^j) - f(\vec{x}_j) \quad k = 1, ..., p \tag{A.7}$$

The resulting scheme becomes

$$\mathbf{Z}_{j+1} = \mathbf{Q}_j + \mathbf{B}_j = \mathbf{Q}_j + [f(\vec{x}_j + h\vec{q}_1^{\,j}) - f(\vec{x}_j), ..., f(\vec{x}_j + h\vec{q}_p^{\,j}) - f(\vec{x}_j)] \tag{A.8}$$

then

$$\mathbf{Z}_{j+1} = \mathbf{Q}_{j+1}\mathbf{R}_{j+1} \tag{A.9}$$

Another way to discretize equation (A.3) is to use the discrete QR: 2nd Order - Explicit Midpoint Rule

$$\mathbf{W}_{1/2} = \mathbf{Q}_0 + \frac{h}{2}\frac{\partial \vec{f}}{\partial \vec{x}^T}(\vec{x}_0)\mathbf{Q}_0 \tag{A.10}$$

$$\mathbf{W}_1 = \mathbf{Q}_0 + \frac{h}{2}\frac{\partial \vec{f}}{\partial \vec{x}^T}(\vec{x}_{1/2})\mathbf{W}_{1/2} \tag{A.11}$$

then

$$\mathbf{Q}_1\mathbf{R}_1 = \mathbf{W}_1 \tag{A.12}$$

To make a Jacobian free method, we must approximate the actions $\frac{\partial \vec{f}}{\partial \vec{x}^T}(\vec{x}_0)\mathbf{Q}_0$ and $\frac{\partial \vec{f}}{\partial \vec{x}^T}(\vec{x}_{1/2})\mathbf{W}_{1/2}$ by appropriate directional derivatives.

$$h\frac{\partial \vec{f}}{\partial \vec{x}^T}(\vec{x}_0)\mathbf{Q}_0 \approx [f(\vec{x}_0 + \frac{h}{2}\vec{q}_1^{\,0}) - f(\vec{x}_0), ..., f(\vec{x}_0 + \frac{h}{2}\vec{q}_p^{\,0}) - f(\vec{x}_0)] \tag{A.13}$$

Thus obtaining

$$\mathbf{Z}_{1/2} = \mathbf{Q}_0 + [f(\vec{x}_0 + \frac{h}{2}\vec{q}_1^{\,0}) - f(\vec{x}_0), ..., f(\vec{x}_0 + \frac{h}{2}\vec{q}_p^{\,0}) - f(\vec{x}_0)] \tag{A.14}$$

Then

$$\begin{aligned} h\frac{\partial \vec{f}}{\partial \vec{x}^T}(\vec{x}_{1/2})\mathbf{Z}_{1/2} \approx \frac{1}{2}[&f(\vec{x}_{1/2} + h\vec{z}_1^{\,1/2}) - f(\vec{x}_{1/2} - h\vec{z}_1^{\,1/2}), ... \\ &, f(\vec{x}_{1/2} + h\vec{z}_p^{\,1/2}) - f(\vec{x}_{1/2} - h\vec{z}_p^{\,1/2})] \end{aligned} \tag{A.15}$$

Thus obtaining

$$\begin{aligned} \mathbf{Z}_1 = \mathbf{Q}_0 + \frac{1}{2}[&f(\vec{x}_{1/2} + h\vec{z}_1^{\,1/2}) - f(\vec{x}_{1/2} - h\vec{z}_1^{\,1/2}), ... \\ &, f(\vec{x}_{1/2} + h\vec{z}_p^{\,1/2}) - f(\vec{x}_{1/2} - h\vec{z}_p^{\,1/2})] \end{aligned} \tag{A.16}$$

$$\mathbf{Q}_1\mathbf{R}_1 = \mathbf{Z}_1 \tag{A.17}$$

Where

$$\vec{x}_{1/2} = \vec{x}_0 + \frac{h}{2}\vec{f}(\vec{x}_0) \tag{A.18}$$

or

$$\vec{x}_{1/2} = \frac{1}{2}(\vec{x}_0 + \vec{x}_1) \tag{A.19}$$

One way to improve the calculation is by using the numerical discretization of directional derivative proposed in [26]

$$\mathbf{F}' \approx \mathrm{Im}(\mathbf{F}(\vec{x}_0 + ih))/h \tag{A.20}$$

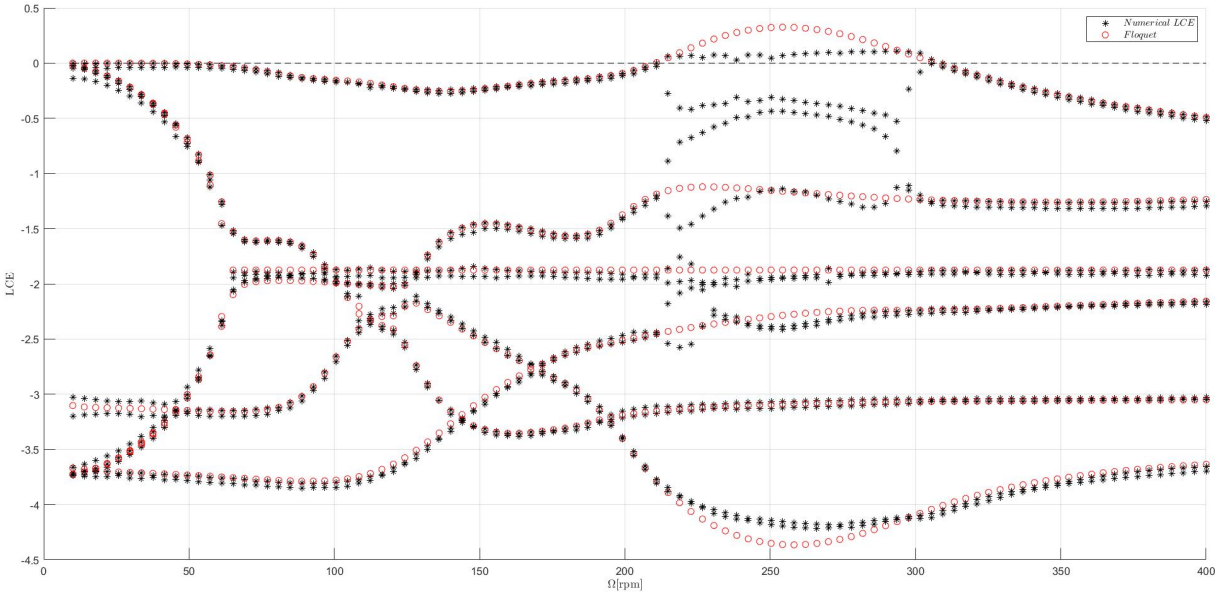

Figure A.1: LCEs obtained by using numerical discretization of the Jacobian matrix, non-isotropic case with $x_0 = 0.1[m]$.

B | Oseledec's Multiplicative Ergodic Theorem

Theorem (Discrete-time Multiplicative Ergodic Theorem). Let T be a measurable function form M to the space of all real $m \times m$ matrices, such that

$$\log^+ ||T(\cdot)|| \in \mathbb{L}^1(M, \rho). \tag{B.1}$$

Then there is a $\Gamma \subseteq M$ with $\rho(\Gamma) = 1$ and such that $T(\Gamma) \subseteq \Gamma$), and the following holds for all $x \in \Gamma$:

1. $\Lambda_x := \lim_{n\to\infty}((T_x^n)^\dagger T_x^n)^{1/2n}$ exists.
2. Let $exp\lambda_x^{(1)} < ... < exp\lambda_x^{(s)}$ be the eigenvalues of Λ_x, where $s = s(x)$, the $\lambda_x^{(r)}$ are real, and $\lambda_x^{(1)}$ can be $-\infty$, and $U_x^{(1)}, ..., U_x^s$ the corresponding eigenspaces. Let $m_x^{(r)} = dim U_x^{(r)}$. The functions $x \to \lambda_x^{(r)}$ and $x \to m_x^{(r)}$ are τ-invariant. Let $V_x^{(0)} = \{0\}$ and $V_x^{(r)} = U_x^{(1)} \oplus ... \oplus U_x^{(r)}$ for $r = 1, ..., s$. Then for $u \in V_x^{(r)} \setminus V_x^{(r-1)}$, $1 \leq r \leq s$,
$$\lim_{n\to\infty} \frac{1}{n} \log(||T_x^n u||) = \lambda_x^{(r)}. \tag{B.2}$$

the demonstration is explained in [15], also with the explanation of the necessary condition for the existence of the limit.

C | Poincaré Map

To study the dynamics of a nonlinear system one instrument that can be used to give an interpretation of the kind of behavior is the Poincaré map. In this case, the periodic Poincaré map is used. A point is saved after a period is passed, in the case of the limit cycle, the Poincaré map should result in a fixed point or orbit. In the case of the Hammond model an orbit is obtained.

For obtaining a Poincaré map first we need to define a section by defining a plane.

$$\langle \hat{n}, (\vec{r} - \vec{r}_0) \rangle = 0 \tag{C.1}$$

$$\langle \hat{n}, \vec{r} \rangle - \langle \hat{n}, \vec{r}_0 \rangle = 0 \tag{C.2}$$

where $\langle \hat{n}, \vec{r}_0 \rangle = d_0$

$$\langle \hat{n}, \vec{r} \rangle - d_0 = 0 \tag{C.3}$$

So to obtain the Poincaré section we need to define the plane by defining $\hat{n}$. Our solution is in 12D plus time so we can define multiple Poincaré maps depending on the chosen subspace. In the numerical method for finding the point at which the solution vector intersects the plane we do if

$$\langle \hat{n}, \vec{x}(t_k) \rangle - d_0 > 0 \text{ and } \langle \hat{n}, \vec{x}(t_{k-1}) \rangle - d_0 < 0$$

(or $\langle \hat{n}, \vec{x}(t_k) \rangle - d_0 < 0$ and $\langle \hat{n}, \vec{x}(t_{k-1}) \rangle - d_0 > 0$. This is due to the periodicity we take only one of the two possibilities.) We save the point and then we do an interpolation from $\vec{x}(t_k)$ and $\vec{x}(t_{k+1})$ to extract a more accurate value of the intersection point. For all the cases stated in the thesis, a Periodic Poincaré map is used.

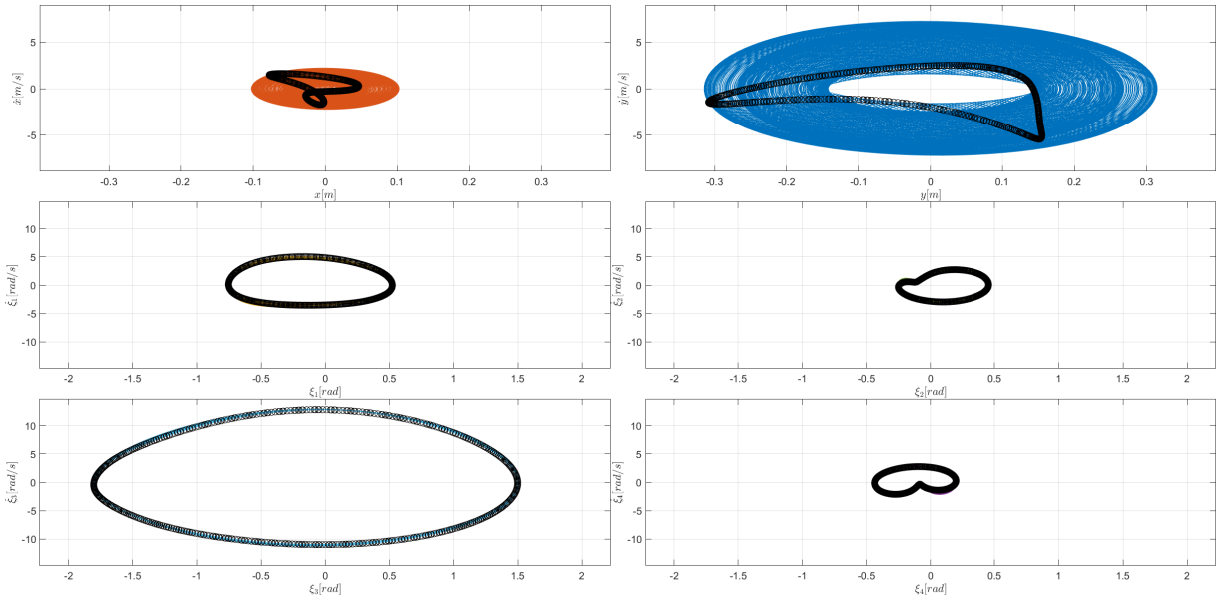

Figure C.1: Phase space of *ad-hoc* solution with one damper inoperative, in unstable conditions ($\Omega = 250$ rpm).

List of Figures

List of Tables

Acknowledgements

First, I would like to acknowledge my family first. My mother and grandmother helped me on this journey by supporting me. My sister and her boyfriend were there all the time when I called them for help. To Fabio, who was always there to lend a hand. With all of the difficulties of this journey, my extended family, Lele, Tujon, Pit, Donny, Conte, Pozzo, Tato, Toe, Mich, and Sapo, supported me day and night. I would also like to acknowledge the friends that were made along the way: Giuly, Tommy, Chri, Otta, Paolo, Bianca, Calin, Elena, Leo, Ale, Gio, Cava, Ludo, Iuri, Luca, Roberto, the staff of Ostello Bello Como, especially Jo for all the beers, and my professor, who was always very helpful and supportive of my work. This journey was like a rollercoaster of emotions with all the friends that were made along the way, the ones that I lost contact with, and the ones that I rediscovered. In the end, it was worth the ticket. As the first part of life ends, a new horizon arises.